STUDY OF $MgB_2$ BASED TRANSMISSION LINE MAGNET FOR ACCELERATOR SYSTEMS

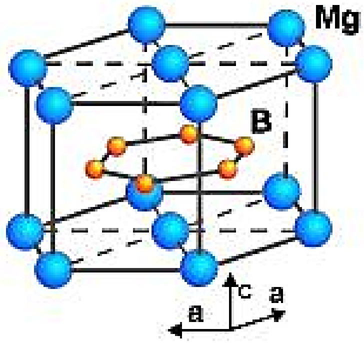


**Dissertation**

Submitted to

The Graduate University for Advanced Studies,SOKENDAI

for the degree of

**DOCTOR OF PHILOSOPHY**

($Accelerator Science$)

**by Mukesh Dhakarwal**

Under the Supervision of
**Dr. Toru Ogitsu**
**Dr. Michinaka Sugano**

December, 10 2019

# Contents

# List of Figures

# List of Tables

# Chapter 1

# Introduction

## 1.1 Background of the Thesis Research Project

Accelerators are key components to provide energetic particles to investigate the structure of the atomic nucleus. Invented in 1930s, by 2017, there were several thousand small and large accelerator systems installed worldwide. With the increasing use of accelerators, not only in the field of particle physics but also in the medical sciences for the cure of several diseases, many smaller accelerator systems will be installed in the future [1].

The superconducting magnet, one of the vital component of the accelerator system. In an accelerator system, magnets are used to produce a strong and stable magnetic field, several type of magnets are used in accelerator system, however dipole and quadrupole are the principle magnets with the prime objective to bend the path of the beam of particle and to focus a beam, gathering the particles close together, respectively. The majority of existing particle accelerators (which uses superconducting magnets) are using low critical temperature ($T_c$) superconductor, mainly niobium titanium (NbTi, $T_c$ = 9.2 K) or niobium tin ($Nb_3Sn$, $T_c$ = 18.2 K), which are primarily operated in liquid helium (LHe) environment at 4.2 K [2,3]. In accelerator field, Large Hadron collider (LHC) is one of the biggest consumer of LHe, which requires several metric tons of LHe to cool down the superconducting magnet system. In the case of any problem (quench – loss of superconducting state) in the accelerator magnet, an enormous amount of LHe gets evaporated and can drastically increase the operation cost. In addition, increasing uses of accelerators and superconducting magnets (mainly MRI scanners) in medical field will increase the demand and supply gap of helium. Due to these compelling reasons, there is a growing demand to develop accelerator systems that can operate in higher temperature range with LHe free and somewhat reduces the cost of the systems [4].

In 2001, superconducting phenomenon in magnesium diboride ($MgB_2$) was observed with relatively high $T_c$ of 39 K [5]. Since then, $MgB_2$ is seen as a promising candidate and a possible replacement of Niobium based superconductor accelerator systems due to its relatively low material and fabrication cost (as compared to high-temperature superconductors (HTS)), with the possibility to operate in the temperature range from 10 K – 25 K, with promising current carrying capacity below 5 T and availability in long length wire conductor [2, 5–7].

J-PARC is one of the leading accelerator facility for several ground-breaking experiments such as T2K, KOTO and upcoming facility (COMET). As these experiments, aim at unprecedented sensitivity in precision and rareness, it is necessary to provide sufficient integrated proton on target **(POT)** which is a product of proton beam power and operation time. Due to increasing demand of POT, limitation in operation time and several upcoming experiments in next decade, a severe shortage of POT is expected. In the future, apart from the ongoing increase in the beam power, one of the possible option is to to upgrade the current facility with a new ring (stretcher ring) in the present tunnel [8]. At present, Fermilab is providing beam simultaneously to multiple facilities by a storage ring, which result in increase in operation time twice as compare to J-PARC.

Construction and operation of magnets is one of the significant challenge in any upgrade in accelerator system. Superconducting combined function magnet with warm iron yoke and superconducting transmission line as primary candidate is an excellent choice for field below 2T. FNAL developed the first transmission line magnet using low-temperature superconductor for the Very Large Hadron Collider [9–14]. A comparatively simple design and compact size make it a suitable possibility to install and operate in smaller space.

Conductor selection is also crucial parameter for manufacturing and operation cost of the magnet system. Advancement in the medium and high temperature superconductors increasing the interest in transmission line technologies using HTS or $MgB_2$ as conductor [15–18]. Industries are also actively developing transmission line for power delivery system using these superconductors [19, 20]. Recently, CERN is also considering $MgB_2$ as the conductor for the transmission line magnet for high luminosity LHC [21].

This thesis, therefore, presents the original research work done for the ***Study of $MgB_2$ Based Transmission Line Magnet for Accelerator Systems***. The following section of *Chapter 1* includes brief introduction to superconductivity and particle accelerators.

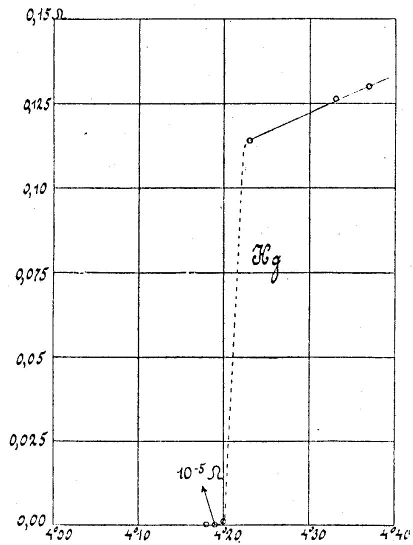


**Figure 1.1:** The first measurement of superconductivity by H. K. Onnes

## 1.2 Superconductivity

1911, the ground-breaking year in the field of Science when famous Dutch scientist Heike Kamerlingh Onnes during his investigation he found that, resistance of mercury (Hg) dropped significantly low which is nearly unmeasurable when cooled to boiling temperature of liquid Helium (4.2 K). H. K. Onnes called this phenomenon 'superconductivity', which is retained since then *figure1.1* shows the first measurement conducted by H. K. Onnes [22].

Since then, in last 10 decades, scientists are continually trying to find new material that shows this phenomenon and efforts are still going on to discover new materials that can show almost zero resistance near the room temperature (RT).

### 1.2.1 Meissner Effect

Apart from the zero dc electrical resistivity of superconducting materials below *($T_c$)*, superconducting materials exhibit another unique characteristic. In 1933, Meissner and Ochsenfeld observed that in a superconducting state, a weak magnetic field ($B$, $B = \mu$ H, where $\mu$ is the magnetic permeability of a material) is expelled from the interior of the bulk superconductor, irrespective of the path used to apply the magnetic field,i.e., $B = 0$ inside the superconductor, as shown by *figure1.2*

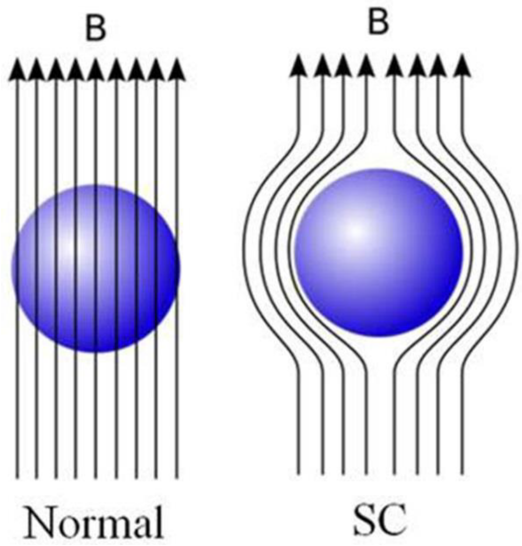


**Figure 1.2:** meissner effect, normal and superconductor

This characteristic of the superconductor is called the Meissner effect. This perfect diamagnetism property of a superconductor is more fundamental than the zero dc electrical resistivity $(\rho)$, i.e., $\rho = 0$ because perfect diamagnetism automatically requires a conductor to be a perfect electrical conductor. The surface supercurrent is primarily responsible for the Meissner effect.

### 1.2.2 London Penetration Depth $(\lambda_L)$ and Coherence Length $(\xi)$

Detailed experiments on field expulsion suggest that when a bulk superconductor placed in an external magnetic field, it cannot produce a perfect surface current which keeps all magnetic fields away from its interior. Some magnetic field always penetrates to certain distance into the bulk superconductor. In 1935, London observed that, while exhibiting the Meissner effect, there was a supercurrent flow within a penetration depth at the surface of the superconductor [28]. London symbolised this penetration depth as

$$\lambda_L = \sqrt{\frac{m}{\mu_0 e^2 n_{se}}} \tag{1.1}$$

where $m$ and $e$ are the mass and charge of an electron, respectively, and $n_{se}$ is the density of the superconducting electrons. According to the London theory, within $\lambda_L$ the magnetic field exponentially decreases with the increasing distance from

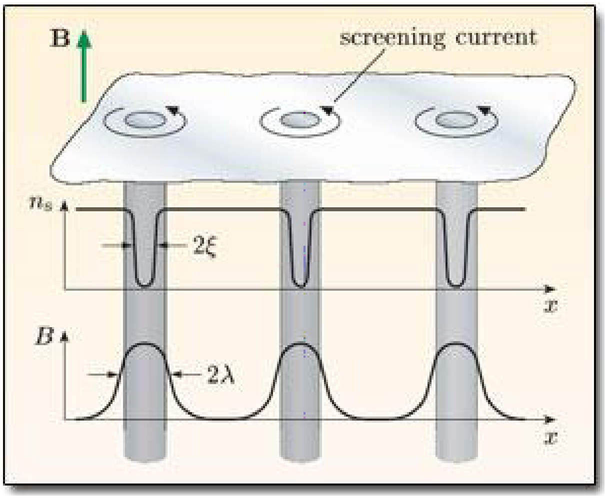


**Figure 1.3:** The density of superconducting electrons, coherence length, and penetration depth inside a superconductor

the edge of the superconducting specimen. The temperature dependence of the $\lambda$(T) can be approximated by

$$\lambda(T)\approx\lambda(0)[1-t^4]^{\frac{1}{2}} \tag{1.2}$$

It was experimentally observed that the $\lambda$ determined experimentally was somewhat larger than $\lambda_L$. In 1955, A. B. Pippard successfully solved this discrepancy by introducing the concept of the coherence length $(\xi)$ by proposing a nonlocal generalization of the London theory [27]. In the nonlocal electrodynamics of the normal metal, the $(\xi_0)$ plays a role similar to the mean free path, *l*. The coherence length $(\xi)$ in the presence of scattering was assuming to be related to that of pure material $(\xi_0)$by

$$\frac{1}{\xi}=\frac{1}{\xi_0}+\frac{1}{l} \tag{1.3}$$

Inside a superconductor, the density of the superconducting electrons changes gradually over a distance $(\xi)$ . Therefore, there is no sharp boundary between superconducting and normal areas within a superconductor. In the core of a superconducting region, $(\xi)$ has a constant value, whereas it gradually decreases on moving inside a normal region and is zero at the centre of a normal region as shown in *figure1.3*.

According to the theory of Ginsburg, Landau, Abrikosov, and Gorkov on classifying types of superconductors, a superconductor is *type I* if$(\xi) > \sqrt{2}\lambda$ , and *type II* if $(\xi) \leq \sqrt{2}\lambda$. The ratio *k*=$\frac{\lambda}{\xi}$ is called the Ginsburg-Landau (GL) parameter [29].

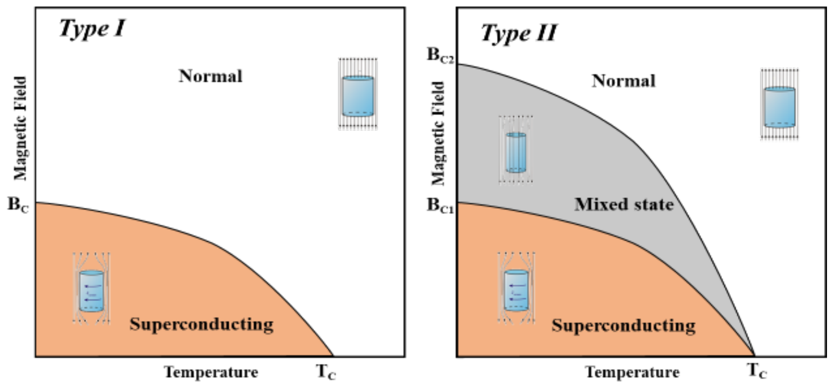


**Figure 1.4:** Magnetic phase diagram for *type I* and *type II* Superconductors

### 1.2.3 Type I and II superconductor

Due to enormous practical consequences results in the finding that there exist two types of superconductors that shows somewhat different response to magnetic fields. According to their diamagnetic properties, superconductors are characterized into two groups, *type I* superconductors and *type II* superconductors.

In *type I* superconductors critical magnetic field *($H_c$)* is a limiting factor as the applied field from outside surpass the $H_c$, material will leave its superconducting state. When the applied field is lower than $H_c$, the material is in Meissner state. According to Meissner effect, if a material is in superconducting state the magnetic field lines are expelled. The magnitude of external field penetrates into the surface of the superconductor depends on the penetration depth which is given by

$$H(x) = H_0 exp(\frac{-x}{\lambda}) \tag{1.4}$$

where, x is the distance from the surface and $\lambda$ is the penetration depth.

*Type I* superconductors are mainly pure metals and have limited practical uses due to low critical magnetic field and high sensitivity.

On the other hand, in *type II* superconductors, shift from normal state to Meissner state is not sudden but goes through a transitional state in which applied field can penetrate through certain local regimes. This is called the vortex state as vortices of the superconducting current surrounded by filaments or cores of normal conducting materials and its shows a mixed state of normal and superconducting regions [23].

If the applied field is increased up to a lower critical field $H_{c1}$, the material expels all the magnetic flux lines. Further increase in the applied up to higher critical field $H_{c2}$, the material is in mixed or vortex state and some flux lines can

| Type I | $T_c$ (K) | $\mu_0 H_c$(T) | Type II | $T_c$ (K) | $\mu_0 H_c$(T) |
|---|---|---|---|---|---|
| Ti (metals) | 0.39 | 0.0100 | Nb(metal) | 9.5 | 0.2* |
| Zr | 0.55 | 0.0047 | NbTi(alloy) | 9.8 | 10.5** |
| Zn | 0.85 | 0.0057 | NbN(metalloid) | 16.8 | 15.3** |
| Al | 1.18 | 0.0105 | $MgB_2$ | 39 | 35-60 |
| In | 3.41 | 0.0281 | $Nb_3Sn$ | 18.2 | 24.5** |
| Sn | 3.72 | 0.0305 | $Nb_3Al$ | 18.7 | 31.0** |
| Hg | 4.15 | 0.0411 | $Nb_3Ge$ | 23.2 | 35.0** |
| V | 5.38 | 0.1403 | $YBa_2Cu_3O_{7-x}$(oxides) | 93 | 150* |
| Pb | 7.19 | 0.0803 | $Bi_2Sr_2Ca_{n-1}Cu_nO_{2n+4}$ | 85-110 | $> 100$* |

**Table 1.1:** Selected type I and type II superconductors and their $T_c$ and $\mu_0 H_c(B_{c2})$

penetrate through the sample. The effect of these flux lines are cancelled out by the supercurrents circulating around the walls of the vortices and net magnetic flux is zero.

In superconducting magnets, to achieve high critical currents, materials with high $B_c$ is prerequisite. As shown in *table 1.1* [24]Type-I superconductors having very low $B_c$ make them inappropriate for the superconducting magnets and giving type-II materials an advantage over type I. Superconductive magnets based on niobium alloys achieving magnetic field of about 20 Tesla, when operate at temperature of 4 K (cooled by liquid helium).

### 1.2.4 Critical surface

The three essential properties of any superconductor are critical current *($T_c$)*, critical magnetic field *($H_c$)*, and critical current density *($J_c$)*.

***Critical temperature ($T_c$)*** is one of the vital property of the superconductors at which the resistivity of the material reduced to value close to zero. Efforts are continuously going on in search to find higher *($T_c$)* superconductors as close as room temperature (RT).

***Critical magnetic field ($H_c$)*** is another curial property, which can affect the performance of the superconductor, as superconductivity cannot sustain in the presence of magnetic field higher than critical value $H_c$ even if we operate at absolute zero temperature. Critical magnetic field is strongly related with the critical temperature of the superconductor. $T_c$ decreases with increase in $H_c$.

***Critical current density ($J_c$)*** is another crucial parameter, which can affect the quality of the superconductor. $J_c$ is the maximum current the superconductor can carry per unit area and it is strongly dependent on the operating temperature. $T_c$ usually decreases with increase in the current flow through the superconductor. As

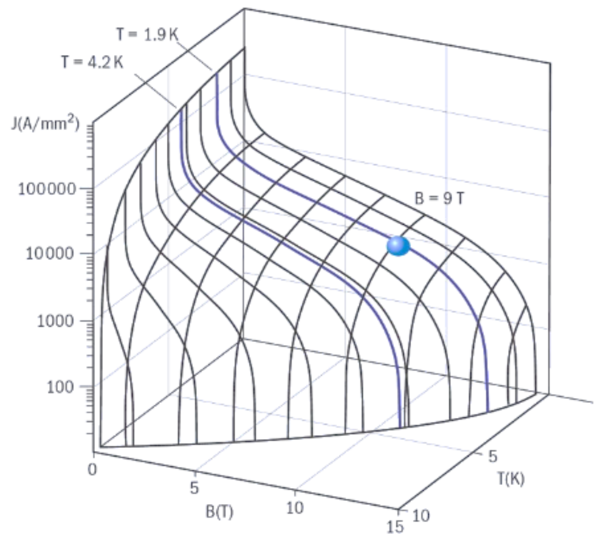


**Figure 1.5:** Critical Surface of Superconductors

flow of current generates magnetic field, higher current density generates higher magnetic field and which results in field on the surface of the conductor exceeding the critical magnetic field *($H_c$)*, eventually vanishes the superconductivity.

Relation between all the three critical parameters plotted in a graph that is defined as critical surface of superconductors as shown in *figure1.5*.

### 1.2.5 Critical Surfaces of Type II Superconductor

1.5 shows the critical surface for a typical Type II superconductor usable for magnets, i.e., magnet-grade superconductor. Superconductivity exists within the phase volume bounded by the surfaces bordered by the function f(J,T,H)

**Critical Current Density, $J_c$**

In a *type II* superconductor, $J_c$ may be enhanced dramatically by means of metallurgical processing. This enhanced $J_c$ performance is generally attributed to the creation of "pinning centers" that anchor the vortices against the $J_c * B$ Lorentz force acting on them. These pinning centers are created in crystal structures by material impurities, metallurgical processes such as cold working to form dislocations, or heat treatment to create precipitates and grain boundaries. Kim and others obtained J(H, T =constant) given by:

$$J_c = \frac{\alpha_c}{H + H_0} \tag{1.5}$$

where $\alpha_c$ and $H_0$ are constants. Note that $\alpha_c$ implies an asymptotic force density

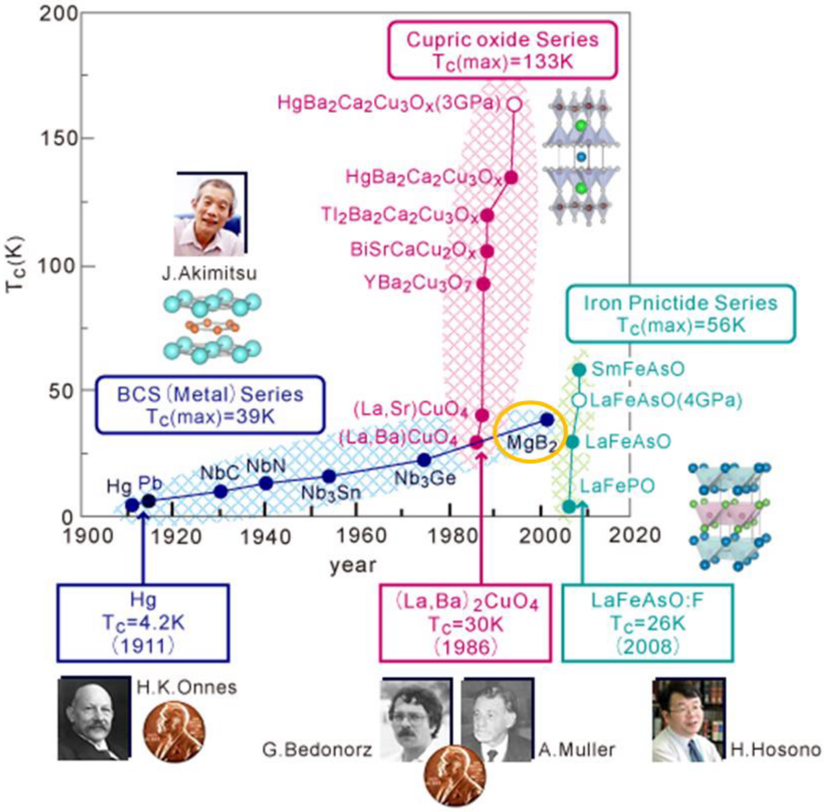


**Figure 1.6:** The trend of the development of superconductors

that balances the Lorentz force density for H $\gg$ $H_0$.

## 1.3 Commercial Superconductors

*Figure1.6* [26]shows the trend in the development of superconducting materials since the discovery of superconducting phenomenon in Hg in 1911 at 4.2 K whereas *table 1.1* shows critical parameters of selected *type I* and *type II* superconductors. Since then, researchers had gained gradual success in next 6 decades with the highest known transition temperature increased from 4 K in Hg to 23 K in $Nb_3Ge$, at a rate of 0.3 K/year.

In last 5 decades this rate is significantly increased due discoveries of new high temperature superconductors. Among the listed superconductors, *type I* superconductors are commercially not viable for magnet construction, *type II* superconductors are mainly used in magnet construction.

As of now, among all the listed superconductors in *table 1.1* [24], NbTi has

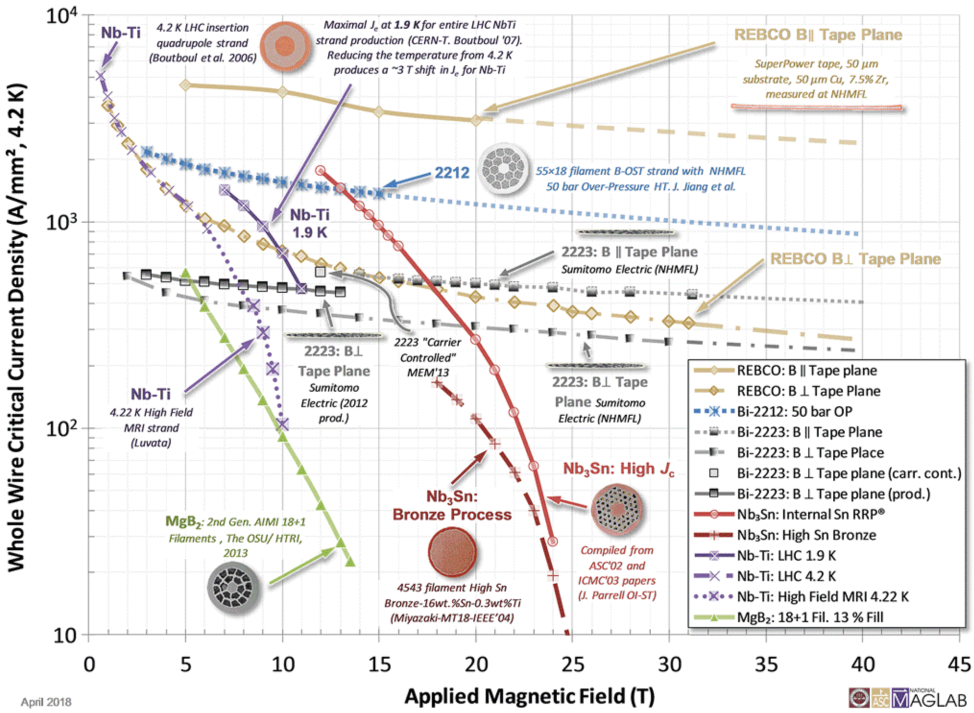


**Figure 1.7:** Engineering Critical Current Density vs. Applied

been the main superconductor used for a commercial magnet fabrication. Due to the difficulty in magnet fabrication and the high strain sensitivity, $Nb_3Sn$ is mostly used for high-field magnet applications. Due to their brittle nature and the high cost of the HTSs such as yttrium barium copper oxide (YBCO) or bismuth strontium calcium copper oxide (BSCCO), they have only been used for certain applications, for example, current leads or an insert magnet, etc. $MgB_2$, which was found to be superconducting in 2001, has been developed very quickly and won its place in the commercial market [5]. Due to its possible LHe-free operation combined with high $T_c$ of 39 K and relatively cheaper fabrication cost compared to HTS, $MgB_2$ has special appeal for commercial applications.

## 1.4 Particle Accelerators

### 1.4.1 Introduction

Accelerators were invented in 1930s to provide energetic particles to investigate the structure of the atomic nucleus. Since then, they have been used to investigate various aspects in the field of particle physics. Their task is to speed up and in-


**Figure 1.8:** KEK and J-PARC accelerator complex layout

crease the energy of a beam of particles by generating electric field that accelerate the particles and magnetic field to align and focus them.

Particle accelerators are of two basic types:

***Linear***- Particles travel through a long, straight track and collide with the target.

***Circular***- Particles travel through a circular tunnel consisting of cavity and magnets until they collide with the target.

In Japan, KEK and J-PARC both accelerator facilities consist of Linear and Circular Accelerators. Layout of KEK and J-PARC as shown in *figure1.8* .

### 1.4.2 Japan Proton Accelerator Research Complex (J-PARC)

As explained in previous section, Japan Proton Accelerator Research Complex **(J-PARC)** is a world's leading research complex with several experimental facilities such as material and life science facility **(MLF)**, neutrino experimental

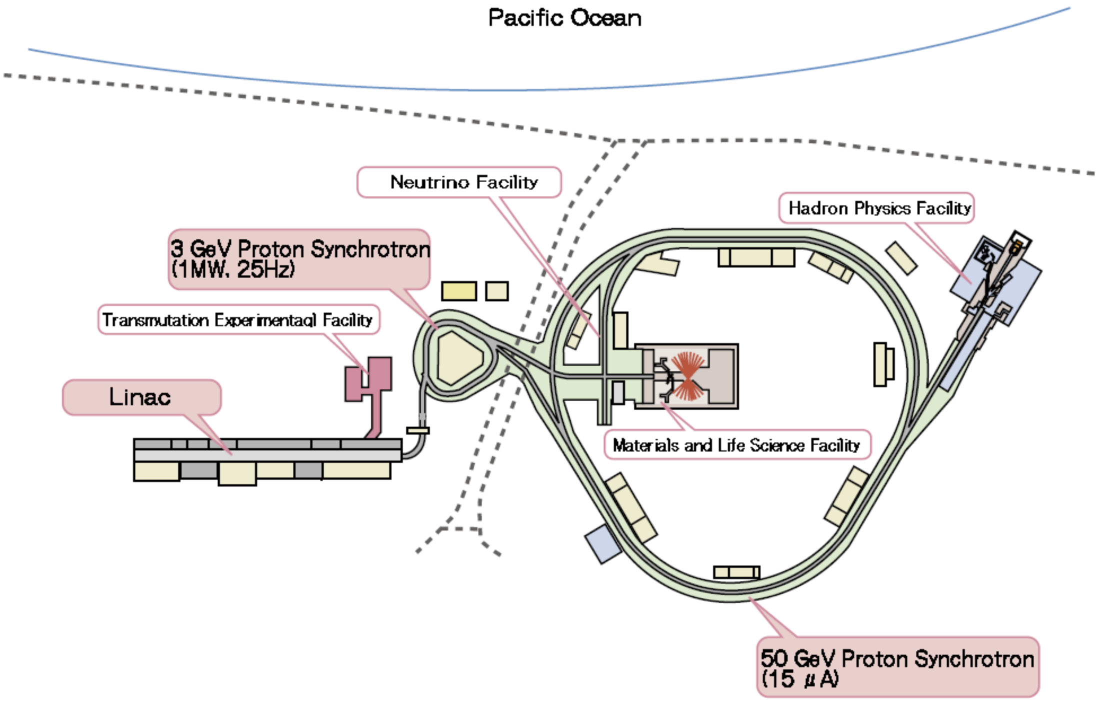


**Figure 1.9:** Layout of J-PARC Accelerator

facility **(NU)** and hadron experimental facility **(HD)**. The main requirement for these experimental facilities is a high intensity proton beam.

J-PARC has three proton accelerators as shown in *figure1.9*, namely the Linac, the Rapid Cycle Synchrotron **(RCS)** and the Main Ring **(MR)**, which serves as feeder of proton on target **(POT)** for three research facilities, to underline the development of advanced science [25].

The Linac accelerates negative hydrogen ions (H-) up to 181 MeV to inject to the RCS. A charge-stripping foil at the injection point of RCS convert the negative ions to protons. The RCS accelerates the protons up to 3 GeV at a repetition rate of 25 Hz, which is then extracted, to the MLF and the MR.

The 1567.5 m long MR, provides 30 GeV high-intensity beams to the NU by fast extraction and to the HD by slow extraction. The MR has a three-fold symmetry with three arc and three straight sections. Each arc section consists eight identical modules with one module consists of four identical bending, four quadrupole, and three chromaticity corrected magnets. Each straight section have a length of 116.1 m, which is dispersion free and consists of seven groups of quadrupole magnets. Steering magnets placed near the quadrupole magnets over the entire length of the MR. The three straight sections are dedicated to injection and beam collimation, slow extraction, and fast extraction respectively. For slow extraction, dedicated electrostatic and magnetic septa, bump magnets, and a slow collimator are placed in the straight section. A horizontal tune is approached to $3Q_x = 67$ resonance line for the slow extraction. Eight resonant sextupole magnets are distributed in the arc sections. All the magnets used in the MR are normal conducting type and of separation function type.

The future is bright with upgrades of T2K (T2K-II and T2HK) and hadron facility experiments, as well as a new flagship lepton flavour violation experiment, COMET, will be online and use the facility in the next decades [8]. With completion of above upgrades, the POT shortage crisis will increase, which can be solved by the use of stretcher ring **(SR)**.

# Bibliography


[1] Harwood Academic Publishers, “Particle Accelerators and Their Uses,“

[2] Massachusetts Institute of Technology, “Monofilament MgB2 wire for MRI magnets,“Master’s thesis (2012)

[3] A. M. Luiz et al., “Overview of Possible Applications of High Tc Superconductors,“ Applications of High-Tc Superconductivity, IntechOpen (2011), Web: https://science.sciencemag.org/content/124/3212/103.

[4] Z. Wang et al., “Development of superconducting magnet for high-field MR systems in China,“ Physica C, vol. 482, pp. 80-86 (2012), Web: https://doi.org/10.1016/0370-2693(69)90525-5.

[5] J. Nagamatsu et al., ”Superconductivity at 39 K in magnesium diboride,” Nature, vol. 410, pp. 63-64, 2001

[6] M. Tomsic et al., ”Overview of MgB2 Superconductor Applications,” Int. J. Appl. Ceram. Technol., vol. 4, pp. 250-259 (2007)

[7] C. Buzea et al., ”Review of the superconducting properties of MgB2,” Supercond. Sci. Technol., vol. 14, pp. 115-146 (2001).

[8] T. Ogitsu et al., ”Design study of superconducting transmission line magnet for J-PARC MR upgrade,” IEEE Transactions on Applied Superconductivity, (2017)

[9] G. Ambrosio et al., ”Design study for a very large hadron collider,” Fermilab-TM-2149, 2001.

[10] H. Piekarz et al., ”A Test of a 2 Tesla Superconducting Transmission Line Magnet System,” IEEE Transactions on Applied Superconductivity, vol. 16, no. 2, pp. 342 - 345, 2006.

[11] Y. Huang et al., ”The development of 100 kA current leads for a superconducting transmission line magnet,” IEEE Trans. Appl. Supercond, vol. 16, no. 2, pp. 457-460, 2006.

[12] G. Velev et al., ”Field quality measurements of a 2-tesla transmission line magnet,” IEEE Trans. Appl. Supercond, vol. 16, no. 2, pp. 1840-1843, 2006.

[13] V. S. Kashikhin et al., ”Test results of a 2 tesla superconducting transmission line magnet obtained with 102 sensors array of hall station,” IEEE Trans. Appl. Supercond., vol. 16, no. 2, pp. 1844-1847, 2006.

[14] G. W. Foster et al., ”Conductor design for the VLHC transmission line magnet,” Proc. Part. Accel. Conf., vol. 1, pp. 182-184, 1999.

[15] O. S. Kozlov et al., ”Application of the superconducting tranmission line to accelerator magnet design,” in Proc. 19th Russ. Accel. Conf., 2004.

[16] A. Milanese et al., ”Concept of a hybrid (normal and superconducting) bending magnet base on iron magnetization for 80-100 km lepton/hadron colliders,” in Proc. Int. Part. Accel. Conf., 2014.

[17] G. W. Foster et al., ”Design and operation of an experimental double-C transmission line magnet,” in Proc. Part. Accel. Conf., 1997.

[18] M. Wake et al., ”Force free design of superferric beam line magnet,” in Proc. Part. Accel. Conf., 2003.

[19] H. Thomas et al., ”Superconducting transmission lines—Sustainable electric energy transfer with higher public acceptance?,” Renewable Sustainable Energy Rev., vol. 55, pp. 59-72, 2016.

[20] H. Thomasa et al., ”Efficiency of superconducting transmission lines: An analysis with respect to the load factor and capacity rating,” Electr. Power Syst. Res., vol. 141, pp. 381-391, 2016.

[21] A. Ballarino, ”Development of superconducting links for the large hadron collider machine,” Supercond. Sci. Technol., vol. 27, 2014.

[22] H. K. Onnes, ”The Resistance of Pure Mercury at Helium Temperatures,” Commun. Phys. Lab. Univ. Leiden, 1911.

[23] Y. Mert, Fabrication and characterization of MgB2 powders and Cu-CLAD MgB2 wires, 2005.

[24] Y. Iwasa, Case studies in superconducting magnets, design and operation issues, New York: Springer, 2009.

[25] ”J-PARC Accelerator,” [Online]. Available: www.j-parc.jp.

[26] http://www.supera.titech.ac.jp

[27] Pippard A B 1953 Proc. Roy. Soc. (London) 547

[28] London F A H 1935 Proc. Roy. Soc. (London) A149 71

[29] T. McConville et al.,”Ginzburg-Landau Parameters of Type-II Superconductors”, in Phys. Rev. 140, A1169.,1965

# Chapter 2

# Stretcher Ring Magnet Design

## 2.1 Two Ring in One Tunnel

For upgrade of the J-PARC Main Ring (MR), we are considering a design to place a stretcher ring (SR) in the present tunnel as shown in *figure 2.1*. The J-PARC tunnel have a height of approximately 3.7 m and existing MR of 1.4 m height, with less than 2 m of space availability for the SR. Taking into account the above parameters, for this upgrade, we need a compact, energy, and cost efficient design. In the present study, the design that is considered for SR is as follow:

i) The SR will be suspended from the ceiling of the MR tunnel and will have the same circumference as of the MR.

ii) To limit the operation cost and optimizing the size, to fit the SR in the present tunnel, the main magnets are superconducting types with combined function of dipole and quadrupole fields [1].

Tunnel cross section with the super-ferric type superconducting combined function magnet are as shown as *figure 2.1*.

### 2.1.1 Approach to design

As previously mentioned in *section 1.4.2*, the J-PARC MR is a 1567.5 m long 3-fold symmetry with 3 arc sections and 3 straight sections shown in *figure 1.9*. Each arc section of SR consists of 8 identical modules similar to MR. As shown in *figure 2.2* each module has combined function magnet that produces dipole and quadrupole field (BMNDCMB, BMNFCMB). It has separated function quadrupole magnets (QFX, QDX). The beam optics of module is shown in *figure 2.2* [1]

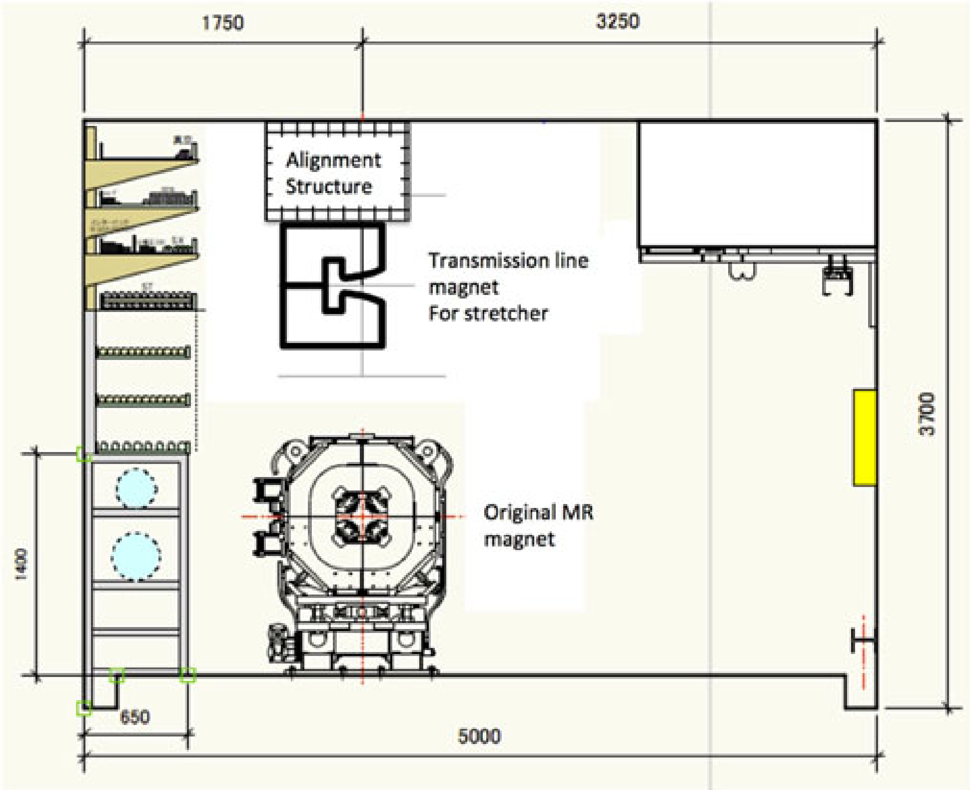


**Figure 2.1:** J-PARC tunnel cross section with transmission line magnet for SR

### 2.1.2 Combined Function Magnet

As described in *section 1.1*, the magnet design considered for the SR is a super-ferric C-shaped magnet powered by superconducting transmission line. The initial design of the iron shape is generated by two-dimensional magnetic potential equation, without taking into consideration the sextupole field [].

$$[\frac{n}{2}\ln(1+\frac{x}{\rho})+1+\frac{n}{2}\frac{x}{\rho}+\frac{n}{4}(\frac{x}{\rho})^2]y = g \tag{2.1}$$

where $\rho$ = 89.381 m and g = 134 mm are the bending radius of the magnet and the gap height on the designed orbit. n=$\frac{\rho}{B}\frac{\partial B}{\partial \rho}$ is the n index of the magnet pole. The pole shape is given by the gap distance y at x position. Since the pole shape is decided by the analytical formula without taking into consideration the sextupole field. The FEM results does not satisfy the specified field. The cross section of combined function magnet is shown in *figure 2.3*. Further, optimization is performed to get the target field parameter in ***chapter 3***.

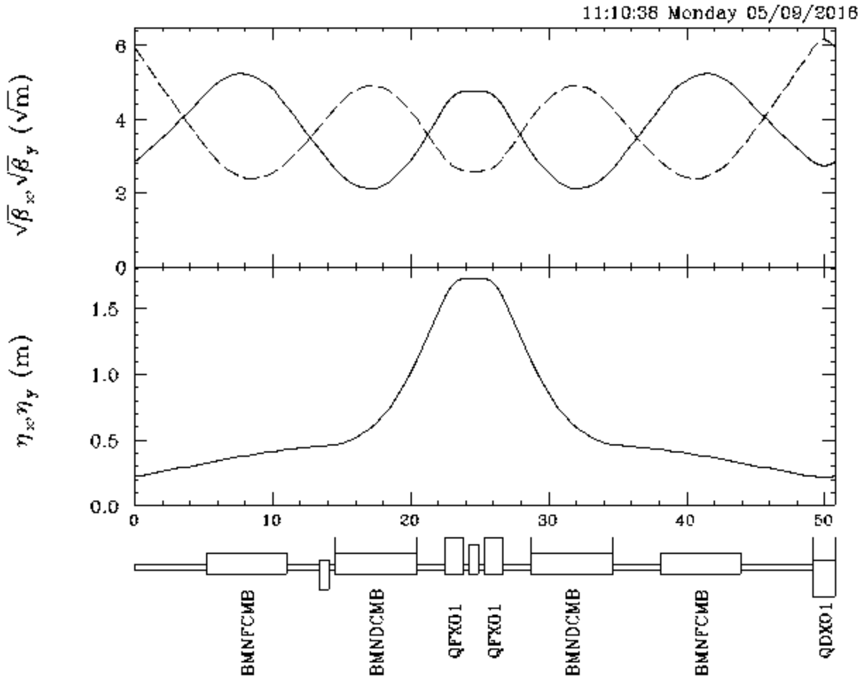


**Figure 2.2:** Beam optics of one arc module in the arc section of the stretcher ring

| Parameter | Expected field | FEM field |
|---|---|---|
| Dipole Field | 1.15 T | 1.15 T |
| Quadrupole Field | -3.14 T/m | -3.8 T/m |
| Sextupole Field | 17 T/m$^2$ | -8.0 T/m$^2$ |
| Magnet Length | 5.85 m | 5.85 m |

**Table 2.1:** Basic parameters of superconducting magnet of Stretcher Ring

The two-transmission line type conductor are placed in the slot between the pole and the return yoke. The cable overall diameter including thermal insulation vacuum jacket is about 130 mm while the inner diameter of the conductor jacket is about 50 mm. Each cable is a set of 4-sub cables each carrying 20 kA with roughly 80 kA current in each cable. In this study, we are considering $MgB_2$ as candidate for the transmission line technology with 10 K 1 MPa gas helium cooling.

### 2.1.3 Transmission Line Geometry

The major component of the transmission line magnet is the 80 kA superconducting transmission line that energizes the magnet. The conductor requirement is

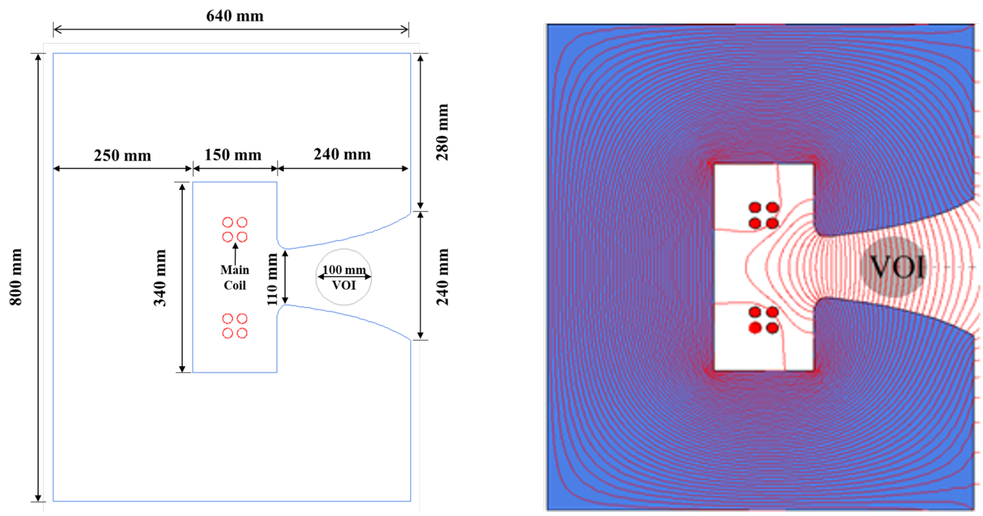


**Figure 2.3:** Cross section of combined function magnet

similar to the cable in conduit design with the following exceptions

Positioning of the conductor inside the iron yoke need to be accurate in order to limit the magnetic decentering forces. In order to achieve this requirement, the superconducting cable is evenly supported by GFRP structure at the center.

In case of quenching, it must have enough copper and thermal mass, which allow dump excess current from 80 kA conductor within seconds. This requires a additional copper which act as stabilizer,and handles the excess heat load apart from the copper inside each $MgB_2$ wire.

The cable must handle the thermal contraction from 300 K to 10 K. This is necessary since the conductor loop is without bellow or expansion joints in a single stretch.

In present design consideration the GFRP support structure is in the center of the 4 sets of transmission line.In order to get free flow of helium gas,a wide cooling jacket is considered in this design.

As mentioned above, the transmission line carry 80 kA current. A 4-set cable geometry is considered in this design. Each set of cable is a combination of 18:1 (SC: Cu) housed in a copper tube which act as a additional stabilizer in case of quench to handle excess heat load, layout of each set in shown in *figure 2.4*.

(a)

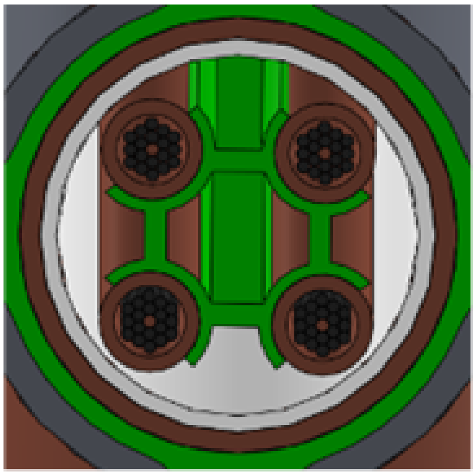

(b)

**Figure 2.4:** Proposed cable assembly for SC Transmission Line (a) Sub-unit of 20 kA cable, (b) 80 kA transmission line

# 2.2 Magnesium Diboride ($MgB_2$)

Magnesium diboride ($MgB_2$) was a quite known compound since 1950s, but in 2001, $MgB_2$ gained a sudden attention when, J. Akimitsu group observed nearly zero resistivity in the compound at a relatively high temperature (39 K) [3]. The binary compound is a combination of two elements: magnesium (Mg) and boron (B) [4] . $MgB_2$ can be economical option as compare to other HTS materials such as BSCCO and REBCO [18,36], due to less expensive material and much simpler fabrication process as HTS have complicated fabrication process with expensive rare earth materials [2].

## 2.2.1 Crystal Structure and Basic Properties of $MgB_2$

$MgB_2$ has a simple hexagonal crystal structure as shown in *figure 2.5* with space group p6/mmm. The lattice parameters of pure $MgB_2$ are a = 3.084 Å and c = 3.524 Å, and the inter-atomic distance is B-B intra-layer 1.780 Å, Mg-Mg intra-layer 3.084 $\AA$, Mg-Mg inter-layer 3.524 $\AA$ and Mg-B 2.5 $\AA$ [4]. The boron atoms are arranged in a honeycomb structure whereas; the Mg atoms are located at the pores of the hexagons. The inter-plane B-B distance is almost double the in-plane B-B distance. The Mg and B layers form ionic bonds by sharing valence

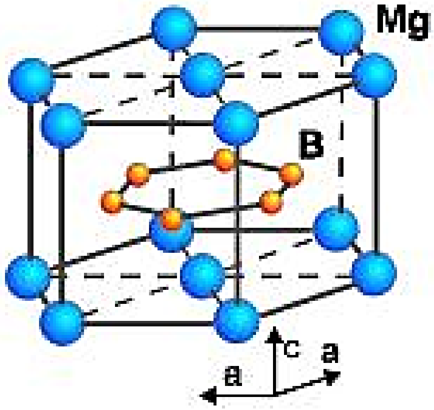


**Figure 2.5:** Crystal structure of $MgB_2$

electrons with each other. The 2D covalent $\sigma$bonds are responsible for holding the B atoms in a plane, whereas the three-dimensional (3D) metallic $\pi$ bonds exist between the layers [5]. It is supposed that the B layers are responsible for the superconductivity in $MgB_2$ [6]. $MgB_2$ follow conventional Bardeen-Cooper-Schrieffer (BCS) superconductivity [7]. This was apparent when the boron isotope B11 was used in the place of B10, and -1 K shift in $T_c$ was observed [8]. The grain size in typical poly-crystalline $MgB_2$ material is from 10 nm - 10 $\mu$m [9]. The anisotropy of $MgB_2$ is from 1.5-5, which is lower than for HTS, which eliminates the need for texturing as for the HTS [10]. The coherence length () of $MgB_2$ is 4 - 5 nm and the penetration depth $\lambda$ is 100-140 nm, with the Ginzburg-Landau (GL) factor k = $\lambda/\epsilon$, where $\epsilon$ is the coherence length, $\approx$ 26 at absolute zero [11]. $MgB_2$ has two superconducting energy gaps $\delta 1$ ($\sigma$) $\approx$ 5 - 7 meV and $\delta$ 2 ($\pi$) $\approx$ 1.5 - 3 meV [12].

Pure $MgB_2$ has a very narrow transition width of less than 1 K with the onset critical temperature ($T_c$-onset) of 39-40 K [3]. Various isovalent and aliovalent atoms with different radii have been substituted to increase $T_c$, but except for zinc (Zn) ($T_c$ increase of 1 K), all other substitutions decrease $T_c$. The normal state resistivity ($\rho(T_c)$) of $MgB_2$ is 0.4 $\mu\Omega$cm, which is much lower than for all commercial superconductors, with a high residual resistivity ratio (RRR) of 20 [14]. The depairing current density of $MgB_2$ is 107 A cm-2 which is only one order lower than for HTS [15]. Pure $MgB_2$ conductor achieves a transport critical current density (Jc) on the order of 106 A cm-2 at 4.2 K in self-field, but 3.8 x 10 4 A cm-2 in 6 T [16]. Pure $MgB_2$ has a low lower critical field, Hc1 (0), of 50 mT, an upper critical field, Hc2, of 15-20 T, and an irreversibility field (Hirr) of 6 - 12 T at 4.2 K [17]. Silicon carbide (SiC) doped $MgB_2$ wires showed Hc2 of about 33

T, which is greater than for Nb3Sn [18].

### 2.2.2 Fabrication of $MgB_2$ Conductors for Magnet Application

$MgB_2$ triggered a great deal of interest in the research community soon after the discovery of its superconductivity in 2001 [3], due to the possibility of its operation in cryogen-free, GHe, or mixed cooling environments. The simple crystal structure, high critical temperature, high Jc, large coherence length, and transparency of grain boundaries to the current flow of $MgB_2$, make it special [4]. These properties of $MgB_2$ offer the further promise of some key large-scale applications [25]. As can be seen in figure 2.1, the $MgB_2$ conductor can open up a new domain of applications for superconducting direct current (DC) magnets, especially below 5 T and 20 K. During the past 15 years, $MgB_2$ has been fabricated in various forms, including single crystals, bulk, thin films, tapes, and wires [20–29].

Different types of $MgB_2$ conductor fabrication techniques have been used, such as PIT technique (in situ and ex situ), CTFF, internal magnesium diffusion (IMD), and local internal magnesium diffusion (LIMD). Together with these, cold high-pressure densification (CHPD), cold isostatic pressure (CIP), and hot isostatic pressure (HIP) during conductor fabrication have also been applied on the laboratory scale, and improvement in the conductor performance has been noticed. Nevertheless, these techniques are not being used for commercial wire production so far. The commercially used wire fabrication techniques are discussed below. The in situ processed $MgB_2$ conductors have been used for this thesis work

### 2.2.3 Powder-In-Tube (PIT) Technique (in-situ and ex-situ)

The powder-in-tube(**PIT**) technique is a well-known method for producing long-length superconductors, due to its simplicity [6, 23]. The fabrication steps in PIT wire fabrication are shown in Figure 2.2. In this method, a suitable metal tube is filled with the precursor powder, and the tube is drawn or rolled into a wire or tape, followed by heat-treatment. Usually, a heat-treatment temperature of 600 - 950 °C.is used with a variety of heating schedules to form well-connected $MgB_2$ filaments. There are two variants of the PIT method, an in-situ and an ex-situ. In an in-situ method, stoichiometric Mg and B are used to fill a suitable metallic tube, such as Cu, niobium (Nb), silver (Ag), nickel (Ni), titanium (Ti), iron (Fe), stainless steel (SS), Cu - Ni, Monel, etc. In an ex-situ method, already formed $MgB_2$ powder is used. For improving Jc, however, further suitable heat-treatment (900-1000 °C.) is also applied in the ex situ case [30]. Due to a possible reaction of Mg with sheath materials such as Ag, Cu, and Ni below 825 °C, and Fe and Ta at 900 °C. Nb is often used as a barrier between the sheath and the $MgB_2$ core in an in-situ process [31]. The requirement for Nb makes an in-situ processed

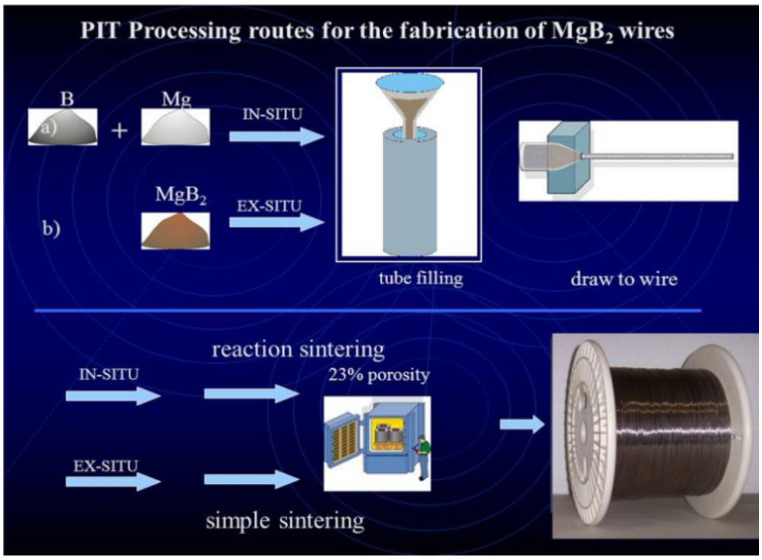


**Figure 2.6:** Fabrication steps for PIT $MgB_2$ wire

conductor quite expensive; therefore, the search for another inexpensive barrier material is indispensable.

The In situ method has several advantages over the ex situ method such as low temperature reaction processes and easy nanoparticle doping to enhance $J_c$ [24]. On the other hand, the ex situ method is more suitable for long lengths, a high packing factor, and complex multi-filamentary conductor geometry [24]. The in situ reaction yields strong inter-grain coupling with a low packing factor, whereas the ex situ process yields tightly packed grains, although their inter-grain coupling is much weaker [32]. At present, many research groups are actively involved in enhancement of the connectivity of grains in ex situ processed conductors [32–35]. Some of the ex-situ processed tapes show Jc values of ≈104 A cm-2 at 20 K in self-field [36]. In the case of ex-situ conductors, heat-treatment normally improves the Jc, but it is still lower compared to in-situ due to relatively poor inter-grain coupling [37–40]. Kario et al obtained $J_c$ of 3.5 x 104 A cm-2 at 9 T and 4.2 K in ex situ $MgB_2$ with 5 percent C addition [41].

# Bibliography


[1] T. Ogitsu et al., ”Design study of superconducting transmission line magnet for J-PARC MR upgrade,” IEEE Transactions on Applied Superconductivity, (2017)

[2] Vinod K, Kumar R G A and Syamaprasad U 2007 Prospects for MgB2 superconductors for magnet application Supercond. Sci. Technol. 20 R1

[3] J. Nagamatsu et al., ”Superconductivity at 39 K in magnesium diboride,” Nature, vol. 410, pp. 63-64, (2001).

[4] C. Buzea et al., ”Review of the superconducting properties of MgB2,” Supercond. Sci. Technol., vol. 14, pp. 115-146 (2001).

[5] P. Ravindran et al., ”Detailed electronic structure studies on superconducting MgB2 and related compounds,” Phys. Rev. B 64 224509 (2001).

[6] S. Jin et al., ”High critical currents in iron-clad superconducting MgB2 wires,” Nature 411 563-5 (2001).

[7] P. Martinez-Samper et al., ”Scanning tunneling spectroscopy in MgB2,” Physica C 385 233-43 (2003).

[8] S. L. Bud’ko et al., ”Boron isotope effect in superconducting MgB2,”Phy. Rev. Lett. 86 1877-80 (2001).

[9] D. C. Larbalestier et al., ”Strongly linked current flow in polycrystalline forms of the superconductor MgB2,”ature 410 186-9 (2001).

[10] S. Hata et al., ”Microstructures of MgB2/Fe tapes fabricated by an in situ powder-in-tube method using MgH2 as a precursor powder,”Supercond. Sci. Technol. 19 161 (2006).

[11] D. K. Finnemore et al., ”Thermodynamic and Transport Properties of Superconducting Mg10B2,”Phys. Rev. Lett. 86 2420-2 (2001).

[12] H. J. Choi et al., ”The origin of the anomalous superconducting properties of MgB2,”Nature 418 758-60 (2002).

[13] www.qm.phy.cam.ac.uk

[14] P. C. Canfield et al., ”Superconductivity in dense MgB2 wires,” Phys. Rev. Lett. 86 2423-6 (2001).

[15] M. N. Kunchur et al., ”Pair-breaking critical current density of magnesium diboride,”Phys. Rev. B 68 064516 (2003).

[16] W. Goldacke et al., ”Development and performance of thin steel reinforced MgB2 wires and lowtemperature in situ processing for further improvements,”Supercond. Sci. Technol. 17 S363 (2004).

[17] Bud’ko S L et al., ”Magnetoresistivity and Hc2 (T) in MgB2,” Phys. Rev. B 63 220503 (2001)

[18] Sumption M D et al., ”Large upper critical field and irreversibility field in MgB2 wires with SiC additions,” Appl. Phys. Lett. 86 092507 (2005).

[19] Tomsic M et al., ”Overview of MgB2 superconductor applications,” Int. J. Appl. Ceram. Technol. 4 250-9 (2007).

[20] Ciszek M et al.,”Effect of carbon substitution on low magnetic field AC losses in MgB2 single crystals,” Physica C 471 794-7 (2011).

[21] Hossain M S A et al.,”Significant enhancement of Hc2 and Hirr in MgB2+C4H6O5 bulks at a low sintering temperature of 600 C,” Supercond. Sci. Technol. 20 L51 (2007).

[22] Xi X X 2009 ”MgB2 thin films,” Supercond. Sci. Technol. 22 043001 (2009).

[23] Kumakura H et al.,”Fabrication and properties of powder-in-tube-processed MgB2 tape conductors,” Physica C 456 196-202 (2007).

[24] Braccini V et al., ”Development of ex situ processed MgB2 wires and their applications to magnets,” Physica C 456 209-17 (2007).

[25] Tomsic M et al., ”Development of magnesium diboride (MgB2) wires and magnets using in situ strand fabrication method,” Physica C 456 203-8 (2007).

[26] Li G 2015 ”Connectivity, doping, and anisotropy in highly dense magnesium diboride (MgB2),” (Ph.D. thesis, The Ohio State University) (2015).

[27] Ionescu A M et al., ”Spark plasma sintered MgB2 co-added with c-BN and C-60,” Mater. Chem. Phys. 170 201-9 (2016).

[28] Wang S et al., ”Preparation, microstructure of B film and its applications in MgB2 superconducting Josephson junction,” Acta Phys. Sinica 65 (2016).

[29] Koparan E T et al., ”Effects of Bi-2212 addition on the levitation force properties of bulk MgB2 superconductors,” Appl. Phys. Mat. Sci. Proc. 122 46 (2016).

[30] Fujii H et al., ”Improved critical current density in ex situ processed carbon-substituted MgB2 tapes by Mg addition,” Supercond. Sci. and Technol. 25 6200405 (2012).

[31] Kumar R G A et al., ”Reactivity of sheath materials with Mg/B in MgB2 conductor fabrication,” Supercond. Sci. Technol. 20 222-7 (2007).

[32] Yamamoto A et al., ”Towards the realization of higher connectivity in MgB2 conductors: insitu or sintered ex-situ?,” J. J. Appl. Phys. 51 010105 (2012).

[33] Pachla W et al.,”Effects of the high-pressure treatment of ex situ MgB2 superconductors,” Supercond. Sci. Technol. 16 7 (2003)

[34] Mizutani S et al.,”Understanding routes for high connectivity in ex situ MgB2 by self-sintering,” Supercond. Sci. Technol. 27 044012 (2014)

[35] Kulich M et al.,”Effect of cold high pressure deformation on the properties of ex situ MgB2 wires,” Supercond. Sci. Technol. 26 105019 (2013)

[36] Grasso G et al.,”Large transport critical currents in unsintered MgB2 superconducting tapes,” Appl. Phys. Lett. 79 230-2 (2001)

[37] lükiger R et al.,”Superconducting properties of MgB2 tapes and wires,” Physica C 385 286- 305 (2003)

[38] Dhallé M et al.,”Transport and inductive critical current densities in superconducting MgB2,” Physica C 363 155-65 (2001)

[39] Siri A S et al.,”Fabrication and characterization of Ni-sheathed MgB2 superconducting tapes,” Int. J. Mod. Phys. B 17 461-7 (2003)

[40] Kováč P et al.,”Progress in electrical and mechanical properties of rectangular MgB2 wires,” Supercond. Sci. Technol. 22 075026 (2009)

[41] Kario A et al.,”Isotropic behavior of critical current for MgB2 ex situ tapes with 5 wt.% carbon addition,” Physica C 483 222-4 (2012)

# Chapter 3

# Field Quality in Accelerator Magnets

## 3.1 Introduction

In accelerator systems, magnets can be broadly categories based on the dominant source field is generated due to the coil or iron yoke and based on that, it is easy to distinguish between coil dominated and iron-dominated magnets.

In C-shaped combined function magnet, the shape of the iron yoke predominantly determines field quality in the magnet aperture. Multipole errors induced in iron dominated are mainly due to the pole shape, and an optimized iron yoke shape can minimize the multipole errors.

The magnetic field quality is an essential factor to keep the particle on stable trajectories. The magnetic field errors in the aperture of the magnets are expressed as the coefficients of the Fourier-series expansion of the radial field components at a given reference radius (in the 2D case). In the 3D case the transverse field components are given at a longitudinal position $z_0$ or integrated over the entire length of the magnetic flux density $B_r$ at a given reference radius $r = r_0$ inside the aperture of a magnet is measured or calculated as a function of the angular position we get the Fourier field expansion.

## 3.2 Field Harmonics

In accelerator system, magnetic field quality in the magnet aperture [1] is usually defined by a set of Fourier coefficients, which are commonly known as field harmonics or multipole coefficient [2, 3]. The overview given in this chapter follows the book called Field Computation for Accelerators [4]. The technique used for calculation of field harmonics is based on finding the general solution that satisfies the Laplace equation in a suitable coordinate system. The integration in the general solution, obtained with the separation of variable technique, are then determined by comparing with the boundary condition.

Starting from the vector potential that satisfies the Laplace equation, $\nabla^2 A_z = 0$, and considering magnet aperture as the problem domain, a general solution can be found

$$A_z(r,\varphi) = \sum_{n=1}^{\infty} r^n (A_n \sin n\varphi + B_n \cos n\varphi) \tag{3.1}$$

The field components can be expressed as

$$B_r(r,\varphi) = \sum_{n=1}^{\infty} n r^{n-1} (A_n \cos n\varphi - B_n \sin n\varphi) \tag{3.2}$$

$$B_\varphi(r,\varphi) = -\sum_{n=1}^{\infty} n r^{n-1} (A_n \sin n\varphi + B_n \cos n\varphi) \tag{3.3}$$

Each value of the integer n in the solution of the Laplace equation corresponds to a specific flux distribution generated by ideal magnet geometries. The three lowest values, n=1,2,3 correspond to the dipole quadrupole, and sextupole flux density distributions. Assuming that the radial component of the magnetic flux density in the Equation 3.1 is measured or calculated at a reference radius $r = r_0$ as a function of the angular position $\varphi$, the Fourier series expansion of the obtained radial field components is [4]

$$B_r(r_0,\varphi) = \sum_{n=1}^{\infty} (B_n(r_0) \sin n\varphi + A_n(r_0) \cos n\varphi) \tag{3.4}$$

where

$$A_n(r_0) = \frac{1}{\pi} \int_0^{2\pi} B_r(r_0,\varphi) \cos n\varphi \tag{3.5}$$

$$B_n(r_0) = \frac{1}{\pi} \int_0^{2\pi} B_r(r_0,\varphi) \sin n\varphi \tag{3.6}$$

Because the magnetic flux density is divergence free it yields that $A_0 = 0$.

In practice, the $B_r$ field components are numerically calculated or measured at a discrete series of points $k$ for a total of $N$ points in the interval (0,2$\pi$) equally spaced $\varphi_k$=$\frac{2\pi k}{N}$, $k$=0,1,2,....N-1. This allows the calculation of two times $N$ Fourier coefficients by the Discrete Fourier Transform (DFT)

$$A_n(r_0) = \frac{2}{N} \sum_{k=1}^{N-1} (B_r(r_0,\varphi_k) \cos n\varphi_k) \tag{3.7}$$

$$B_n(r_0) = \frac{2}{N}\sum_{k=1}^{N-1}(B_r(r_0,\varphi_k)\sin n\varphi_k) \tag{3.8}$$

which establish a relation among field components and the multipole coefficients $A_n(r_0)$ and $B_n(r_0)$ at a given reference radius $r_0$. The components of $B_n(r_0)$ and $A_n(r_0)$ are called normal and skew multipole coefficients of the field. Field components at any radius $r$ are given by [4]

$$B_r(r,\varphi) = \sum_{n=1}^{\infty}(\frac{r}{r_0})^{n-1}(B_n(r_0)\sin n\varphi + A_n(r_0)\cos n\varphi) \tag{3.9}$$

$$B_\varphi(r,\varphi) = \sum_{n=1}^{\infty}(\frac{r}{r_0})^{n-1}(B_n(r_0)\cos n\varphi + A_n(r_0)\sin n\varphi) \tag{3.10}$$

Where $B_r(r_0,\varphi)$ and $B_\varphi(r_0,\varphi)$ denote the radial and tangential field components. Uppercase notation defines the normal $B_n(r_0)$ and skew $A_n(r_0)$ multipole coefficients. It is common practice to normalize the multipole coefficients with respect to the main field component $B_N(r_0)$, denoted in lowercase letters, expressed in a reference frame where the main skew component is zero. In case of the radial field component, this yields,

$$B_r(r,\varphi) = B_N\sum_{n=1}^{\infty}(\frac{r}{r_0})^{n-N}(b_n(r_0)\sin n\varphi + a_n(r_0)\cos n\varphi) \tag{3.11}$$

Applying the following trigonometric functions, $\cos\varphi + \sin\varphi^n$=$(e^{i\varphi})^n$= $e^{in\varphi}$= $\cos n\varphi + i\sin n\varphi$, n $\in \mathbb{Z}$ the magnetic field in Cartesian coordinates components can be expressed as:

$$B_x(r,\varphi) = \sum_{n=1}^{\infty}(\frac{r}{r_0})^{n-1}(B_n(r_0)\sin(n-1)\varphi + A_n(r_0)\cos(n-1)\varphi) \tag{3.12}$$

$$B_y(r,\varphi) = \sum_{n=1}^{\infty}(\frac{r}{r_0})^{n-1}(B_n(r_0)\cos(n-1)\varphi + A_n(r_0)\sin(n-1)\varphi) \tag{3.13}$$

where the normal and skew multipole coefficients $B_n(r_0)$, $A_n(r_0)$ are given in tesla at a reference radius $r_0$. They are often combined in the complex notation $C_n$=$B_n(r_0) + iA_n(r_0)$.

By definition for accelerator magnets, the normal components indicate a vertical field in the horizontal plane while the skew terms indicate horizontal field. In

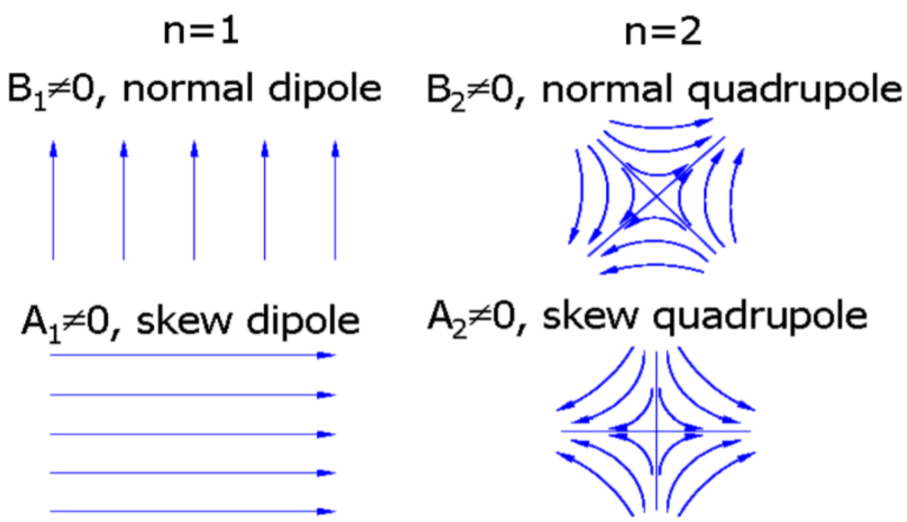


**Figure 3.1:** Field lines of normal and skew dipole and quadrupole magnets: (above-left): normal dipole field lines; (below-left): skew dipole lines; (above-right): normal quadrupole field lines; and (below-right): skew quadrupole field lines

3.1, the field lines for normal and skew dipoles $(B_1, A_1)$ and quadrupoles $(B_2, A_2)$ are shown. Multipole coefficients, from different measurement devices for example, must be compared at the same reference radius $r_0$. The reference radius $r_0$ is an important concept for accelerator magnets and it is usually chosen as 2/3 of the magnets aperture. By choosing a complex plane $(x, y)$, the harmonic can be expressed in terms of the complex variable $z$=$x + iy$ [].

$$B(z) = B_y(z) + iB_x(z) = \sum_{n=1}^{\infty} C_n(z)(\frac{r}{r_0})^{n-1} \tag{3.14}$$

The field quality, described as relative errors with respect to the main field component $B_M$ at the reference radius $r_0$, is given by

$$c_n = b_n + ia_n = 10^4 \frac{C_n}{B_M} \tag{3.15}$$

## 3.3 Optimization of Iron Yoke using SVD

As mentioned in section 2.1.3 , the design obtained using the numerical formula is not satisfying the required field quality. In iron dominated magnet system, pole shape of iron yoke plays an important role in defining the field quality in the beam area which is also called volume of interest (VOI), VOI in this design study is 10 cm in diameter with a target dipole field of 1.15 T, quadrupole field of -3.14 T/m and sextupole field of 17 T/m$^2$

Optimizing the magnet pole contour is an iterative process requires the use of 2-dimensional analysis code/software and mathematical technique to process the data. In order to get the optimized pole shape for the target field, we are using singular value decomposition (SVD) technique and OPERA 2D software to get the field components for the given pole shape.

The pole shape for target field is determined by solving a system of equations formed with a non regular matrix A whose elements are response from points of shimming on pole to the magnetic field on the VOI, using SVD regularization,the response matrix A is then factorized into the product of three matrices $A = U\lambda V^T$ where the columns of U and V are orthogonal and the matrix $\lambda$ is diagonal with positive real entries.

In order to get the target field in VOI , in this method we tunes the eigenmode strengths to determine the amplitude of shimming points.

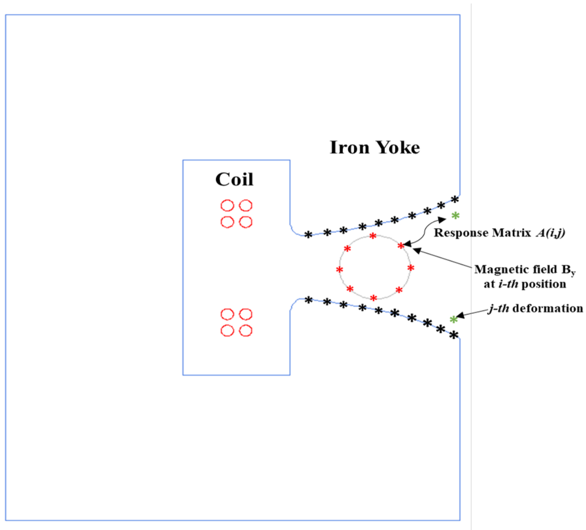


**Figure 3.2:** Geometry for shimming calculation

### 3.3.1 Data Representation

The first step is to convert an analytical or non-analytical design optimization problem formulation into response matrix A. The response matrix A, derived from the shimming points on the yoke pole tip and magnetic field evaluation point (MFEPs) over the 10 cm Volume of interest (VOI). Considering the jth shimming point $D_j$ produces the magnetic field $B_i$(T) at the $i^{th}$ point in the VOI, the relationship is

$$B_i = A_{ij} D_j \tag{3.16}$$

where A is the response matrix.
The response matrix is formed by the difference in the magnetic field before and after iron pole shimming.

$$A = B_y - B_{y0} \tag{3.17}$$

$$A = \begin{pmatrix} A_{1,1} & A_{1,2} & \cdots & A_{1,j} \\ A_{2,1} & A_{2,2} & \cdots & A_{2,j} \\ \vdots & \vdots & \ddots & \vdots \\ A_{i,1} & A_{i,2} & \cdots & A_{i,j} \end{pmatrix}$$

here m=60 as number of MFEP and n=46 as number of shimming points on the pole

### 3.3.2 Error Vector ($B_{err}$)

The second step is to determine the error in the VOI field components to the target field for un-optimized pole shape. In order to determine the error vector, the target fields for which optimization is to be performed need to be decided.
For present design optimization, the target field have dipole and quadrupole field components as $B_{dipole}$=1.15 T and $B_{quad}$ = -3.14 T/m. Error vector can be represented as

$$B_{err} = B_{i0} - B_{dipole} - B_{quad} \tag{3.18}$$

where, $B_{i0}$ is the initial field at magnetic field evaluation points without deformation.

$$B_{err} = \begin{pmatrix} B_{err1,1} \\ B_{err2,1} \\ \vdots \\ B_{erri,1} \end{pmatrix}$$

### 3.3.3 Performing SVD on the data matrix

The third step is to apply the singular value decomposition (SVD) regularization on the response matrix A.

$$A = U\lambda V^T \tag{3.19}$$

where V$_i$ , U$_i$, and $\lambda_i$ (T/A) form a set of an eigenmode.They are eigenvectors of pole deformation, magnetic field distribution, and a singular value.

$$U = \begin{pmatrix} U_{1,1} & U_{1,2} & \cdots & U_{1,j} \\ U_{2,1} & U_{2,2} & \cdots & U_{2,j} \\ \vdots & \vdots & \ddots & \vdots \\ U_{i,1} & U_{i,2} & \cdots & U_{i,j} \end{pmatrix}$$

$$\lambda = \begin{pmatrix} \lambda_{1,1} & \cdots & 0 \\ \vdots & \ddots & \vdots \\ 0 & \cdots & \lambda_{i,j} \end{pmatrix}$$

$$V = \begin{pmatrix} V_{1,1} & \cdots & V_{1,j} \\ \vdots & \ddots & \vdots \\ V_{i,1} & \cdots & V_{i,j} \end{pmatrix}$$

### 3.3.4 Eigenmode Strength $(P_i)$

The fourth step is to determine eigenmode strength from the decomposed matrix U and error field $B_{err}$. Eigenmode strength is determined by

$$\sum \frac{(B_{err} * U_i)}{\sqrt{n_p}} \tag{3.20}$$

$B_{err}$ is the error vector, $U_i$ is the orthonormal matrix where $1 \leq i \leq n_p$ ($n_p$ is number of shimming points) and $N_p$ is number of MFEPs i.e 60 in our case. Eigenmode strength is one of the crucial parameter which helps in determines the eignmode to be used in the iterative process.

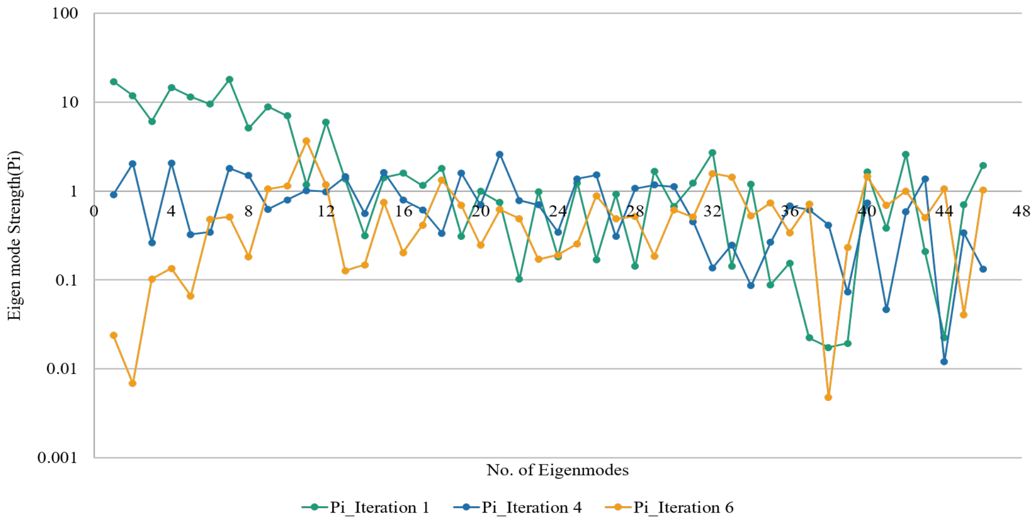


**Figure 3.3:** Reduction in eigenmode strength of higher number of eigenmode with iterative steps

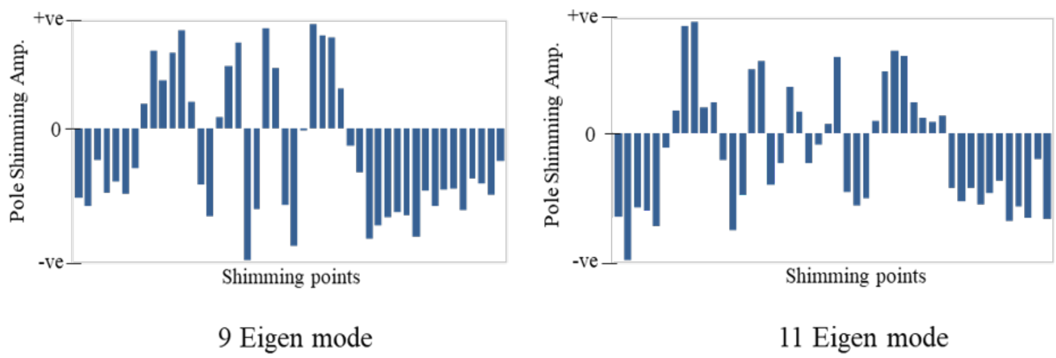


**Figure 3.4:** Comparison of different eigenmode

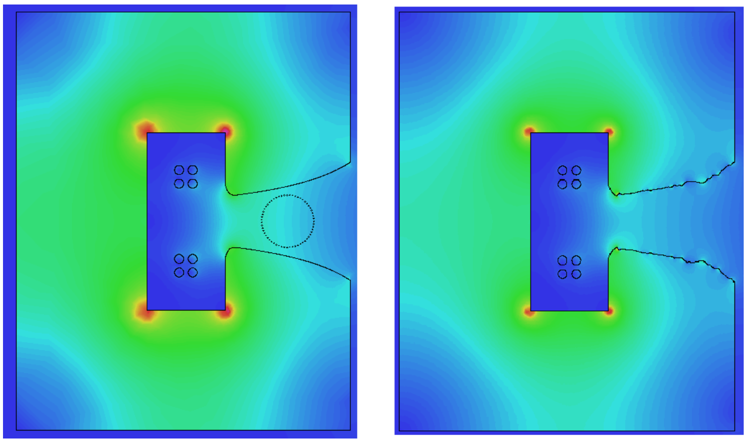

**Figure 3.5:** Pole shape shimming after iterative process

### 3.3.5 Pole Shimming Amplitude $(\Delta D)$

The fifth step is to determine the shimming amplitude in the pole shape: The eigenvectors obtained in step 2 form bases for the distribution and the new pole shape can be obtained as combination based on the eigenmode strength. Based on the eigenmode strength calculated in step 4 , the solutions are obtained using only low-ordered (large singular value) eigenmodes.

$$\sum \frac{V_i * P_i * \sqrt{n_p}}{\lambda_i} \tag{3.21}$$

Parameters mentioned in table still need further iteration in order to make design feasible for the manufacturing process.

| Multipoles | Initial | Iteration 8 | Target field |
|---|---|---|---|
| B1 | 1.1512 T | 1.15 T | 1.15 T |
| B2 | -0.1944 T (-3.88 T/m) | -0.1565 T (-3.13 T/m) | -3.14 T/m |

**Table 3.1:** Field variation in 5 cm reference radius (VOI) by SVD optimization

### 3.3.6 Improved method

In order to reduce the complexities in pole profile and make it commercially feasible we had take a improved approach, the pole shimming amplitude generated in step 5, instead of adding $(\Delta D)$ of 46 shimming point we divided 46 shimming

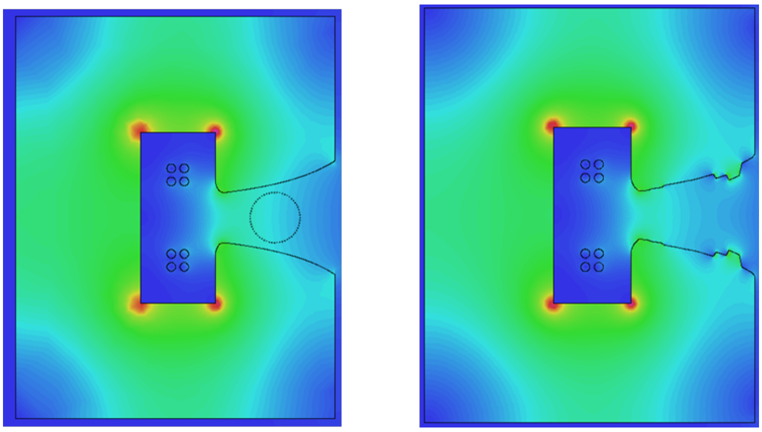

**Figure 3.6:** Pole shape shimming after improved iterative process

points into pair of 5 and added average of pole shimming amplitude. By considering this approach we are successfully able to reduce the complex pole profile and also able to get the target field quality as shown in

| Multipoles | Initial | Iteration 14 | Target field |
|---|---|---|---|
| B1 | 1.1512 T | 1.15 T | 1.15 T |
| B2 | -0.1944 T (-3.88 T/m) | -0.156 T (-3.12 T/m) | -3.14 T/m |
| B3 | -3.89E-03 T (-1.56 T/m$^2$) | 0.43 T (17.2 T/m$^2$) | 17 T/m$^2$ |

**Table 3.2:** Field variation in 5 cm reference radius (VOI) after improving method

In order to validate the above mentioned optimization steps, figure 3.7 shows convergence of combined function profile to the dipole field profile.

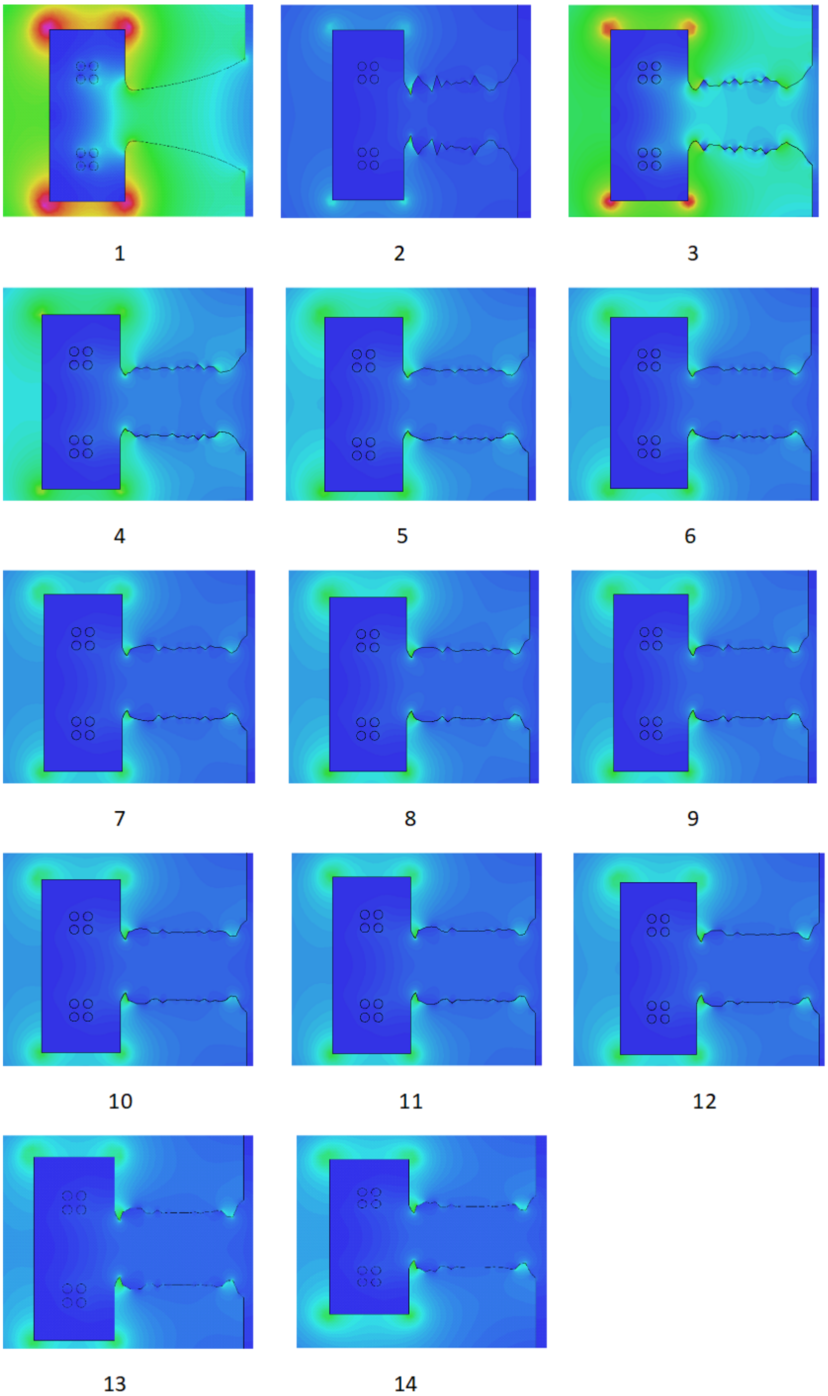


**Figure 3.7:** Iterative pole profile convergence combined function to dipole

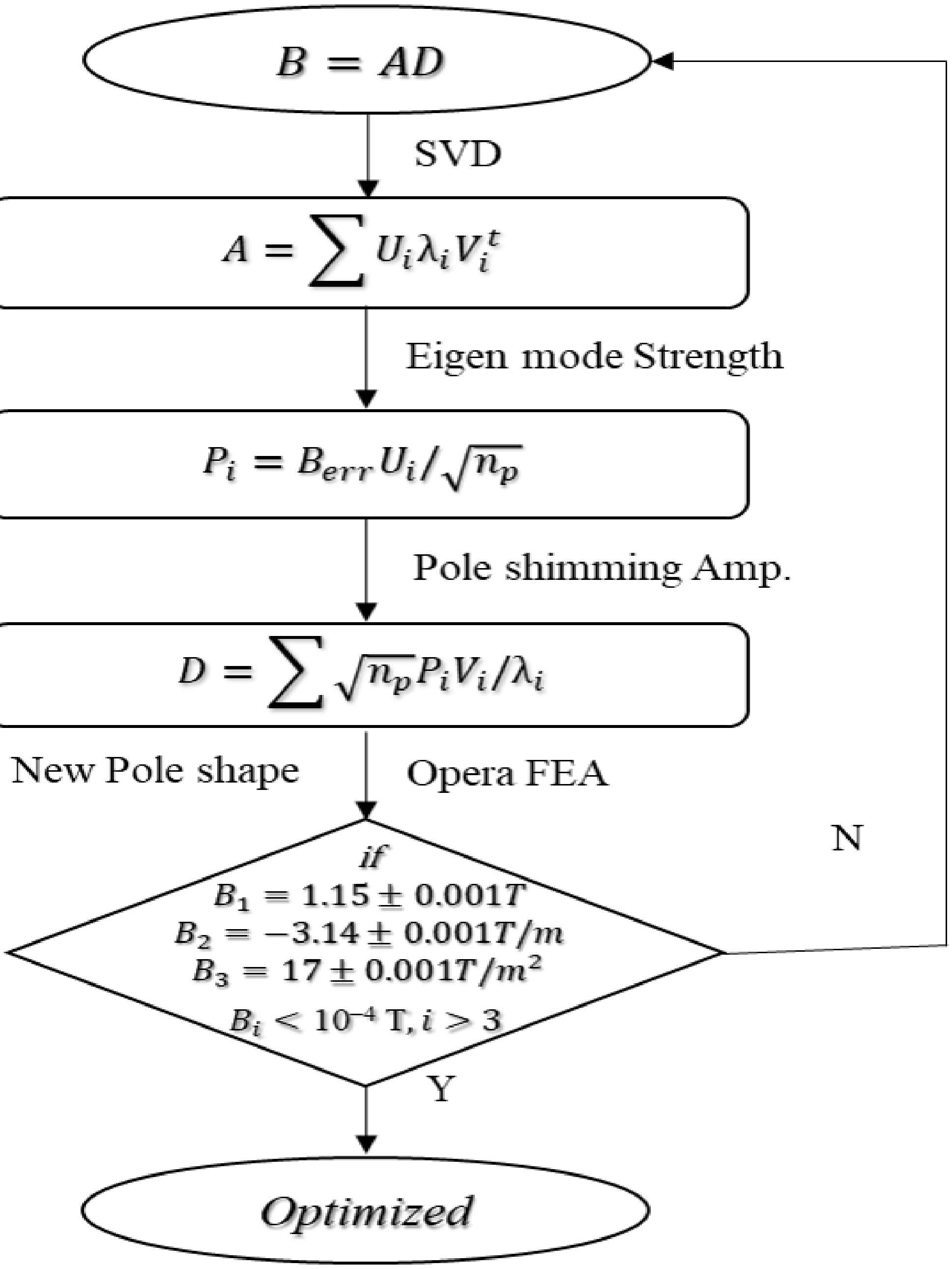


**Figure 3.8:** Singular value decomposition algorithm

## 3.4 Conductor movement effect

Magnetic field quality can be degraded by several factors depending on assembly and operation condition. Misalignment during assembly process can be control by careful assembly. Operation condition are difficult to control, in order to minimize the effects of conductor movement on the magnetic field, allowable tolerance need to be checked. The tolerance in transmission line position and top and bottom asymmetries, FEM analysis using Opera 2D simulation is done. We had calculated field with the displacement of top conductor in both X and Y direction up to 5 mm from the top and bottom symmetry state, keeping bottom conductor at initial position.

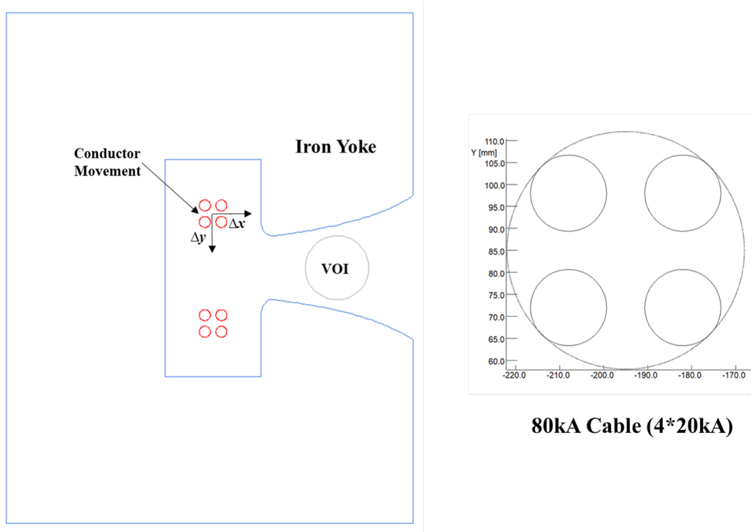


**Figure 3.9:** Schematics of iron yoke with transmission line conductor and displacement direction of conductor

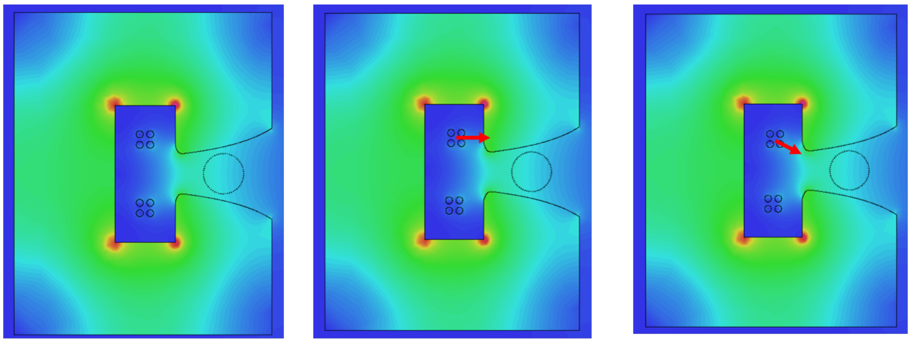

Top conductor (Δx=0, Δy=0)
Bottom conductor (Δx=0, Δy=0)

Top conductor (Δx=-5, Δy=0)
Bottom conductor (Δx=0, Δy=0)

Top conductor (Δx=-5, Δy=-5)
Bottom conductor (Δx=0, Δy=0)

**Figure 3.10:** Movement of conductor in x and y direction

| Conductor displacement | B1 | B2 | B3 | B4 | B5 |
|---|---|---|---|---|---|
| (0,0),(0,0) | 1.1510 | -0.1945 | -4.02E-03 | 2.47E-03 | -2.20E-03 |
| (5,0),(0,0) | 1.1510 | -0.1945 | -4.04E-03 | 2.47E-03 | -2.20E-03 |
| (5,5),(0,0) | 1.1510 | -0.1945 | -4.02E-03 | 2.47E-03 | -2.20E-03 |
| Conductor displacement | A1 | A2 | A3 | A4 | A5 |
| (0,0),(0,0) | -1.69E-05 | 1.16E-05 | -9.80E-06 | -8.02E-06 | 1.10E-05 |
| (5,0),(0,0) | 2.74E-04 | -2.06E-04 | 1.04E-04 | -4.93E-05 | 1.74E-05 |
| (5,5),(0,0) | 1.26E-04 | -8.78E-05 | 3.81E-05 | -2.61E-05 | 1.80E-05 |

**Table 3.3:** Multipole variation (normal and skew) in 5 cm reference radius due to conductor movement

## 3.5 Summary

In this chapter we had described the methodology of optimizing iron pole shape to get the target field quality in the 10 cm diameter volume of interest using singular value decomposition and OPERA 2D and also checked the effects of the transmission line conductor movement on the field quality in order to determine the maximum allowable displacement without degrading the target field quality.

Optimization using SVD is a iterative method based reduction of eigenmode strengths by taking into consideration only the number of eigenmode with higher eigenmode strength and neglecting all the eigenmodes with low eigenmode strength. In our study we had taken 46 shimming points on the iron pole which gives the field components in the VOI. Applying SVD on the response matrix A generated using the difference in the field quality due to change in amplitude of each shimming point on the pole gives a product of three matrices $U$,$\lambda$ and $V^T$, which are used to determine the eigenmode strength and change in each shimming point amplitude, which are used for the successive iterations.

Since the cable is subjected to large amount of forces which can cause movement in the transmission line conductor, we have to take into consideration the maximum allowable displacement in order to limit all higher order field components in the range of $10^{-4}$ T.In this study we had checked the change in the field components with a maximum displacement of conductor by 5 mm in both X and Y direction.

# Bibliography

[1] L. Evans and P. Bryant, LHC Machine. JINST 3 S08001, 2008.

[2] L. Walckiers, The harmonic-coil method, part 1 and 2. presented at the CERN Accelerator School: Magnetic measurement and alignment, Montreux, Switzerland, CERN-92-05, 1992.

[3] L. Bottura, Standard Analysis Procedures for Field Quality Measurement of the LHC Magnets - Part I: Harmonics. Internal Note, LHC-MTA-IN-97-007, 1997.

[4] S. Russenschuck, Field Computation for Accelerator Magnets. Analytical and Numerical Methods for Electromagnetic Design and Optimization. WILEY-VCH Verlag GmbH, Weinheim, 2010.

# Chapter 4

# Electromechanical Properties of $MgB_2$

## 4.1 Introduction

$MgB_2$ wires are amalgam of brittle (ceramic) superconducting $MgB_2$ filaments placed in one or more ductile metallic sheaths. Consequently, the performance of $MgB_2$ wire is not only constrained to the electrical properties $(I_c)$ of the superconductor but also affected by the resulting mechanical stresses during fabrication and operations. The mechanical behavior of multi-filament $MgB_2$ wire is highly influenced by fiber characteristics, by the strength and nature of interface and by matrix hardening characteristics.

Since superconducting magnets have high field and current density as shown in figure 4.3 (around 65 kA current). Superconducting transmission line or coils experiences large amount of stresses which can cause several effects in a magnet system like degradation of coil and field quality, and can also trigger quench.

Superconducting magnet system, having several components that are operated at temperature range 4.2 K - 20 K. Since the fabrication and assembly is done at room temperature,material selection is a crucial parameter as different materials goes under thermal contraction during cool-down cycles. During material selection and fabrication and assembly the following things need to be considered:

(i)Minimum tensile stresses on the superconductor

(ii)minimize mechanical degradation of the materials

(iii)Sufficient ratio of normal conductor to protect magnet in case of quench.

### 4.1.1 Electromagnetic forces

A charged particle *q* moving with speed *v* in the presence of an electric field *E* and a magnetic field *B* experiences the Lorentz force, which is given by

$$F[N] = q(E + \mathrm{v} * \mathrm{B}) \tag{4.1}$$

In the same way, a conductor element carrying current density *j* in the presence of a magnetic field *B* will experience the force density

$$f_L[N.m^{-3}] = \mathrm{j} * \mathrm{B} \tag{4.2}$$

The Lorentz force is a body force, i.e. it acts on all the parts of the conductor, as does the gravitational force. The total force on a given body can be computed by integration:

$$F[N] = \int\int\int f_L dv \tag{4.3}$$

The magnetic energy density u stored in a region without magnetic materials ($\mu_r$ = 1) in the presence of a magnetic field *B* is

$$u[J.m^{-3}] = \frac{B.H}{2} = \frac{\mathrm{B}^2}{\mu_0} \tag{4.4}$$

The total energy *U* can be obtained by integration over all the space, by integration over the coil volume, or by knowing the so-called self-inductance *L* of the magnet:

$$U[J] = \int\int\int_{all} \frac{B.\mathrm{H}}{2} dv = \int\int\int_{coil} A.\mathrm{j}dv = \frac{1}{2}LI^2 \tag{4.5}$$

### 4.1.2 Stress and strain

The mechanical properties of materials are determined by performing carefully designed laboratory experiments that replicate as nearly as possible the service conditions. In real life, there are many factors involved in the nature in which loads are applied on a material. The following are some common examples of modes in which loads might be applied: tensile, compression, and shear. These properties are important in materials selections for mechanical design. Other factors that often complicate the design process include temperature and time factors. In continuum mechanics, stress is a physical quantity which expresses the internal pressure that neighboring particles of a continuous material exert on each other. As shown in *figure 4.1(a)*, when the forces are perpendicular to the plane, the stress is called normal stress ($\sigma$); when the forces are parallel to the plane, the stress is called shear stress ($\tau$). Stresses can be seen as the way a body resists

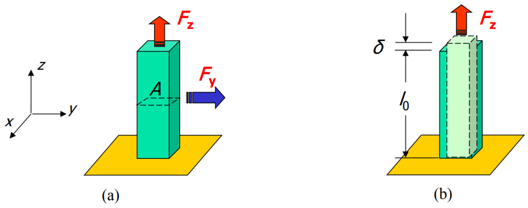


**Figure 4.1:** (a) Normal and shear stresses (b) Strain

the action (compression, tension, sliding) of an external force. A tensile (pulling) stress is considered as positive, and is associated with an elongation of the pulled body. As a consequence, a compression (pushing) stress is negative and is associated with a body contraction [1]. The normal and shear stresses are given by

$$\sigma[Pa] = \frac{F_z}{A} \tag{4.6}$$

$$\tau[Pa] = \frac{F_y}{A} \tag{4.7}$$

A strain $\epsilon$ is a normalized measurement of deformation representing the displacement $\delta$ between particles in the body relative to a reference length $l_o$

$$\epsilon = \frac{\delta}{l_o} \tag{4.8}$$

According to Hookes law (1678), within certain limits, the strain $\epsilon$ of a bar is proportional to the exerted stress $\sigma$. The constant of proportionality is the elastic constant of the material, the so-called modulus of elasticity E, or young modulus:

$$\epsilon = \frac{\delta}{l_o} = \frac{\sigma}{E} = \frac{F}{AE} \tag{4.9}$$

The Poisson ratio $v$ is the ratio of transverse to axial strain:

$$v = -\frac{\epsilon_{transversal}}{\epsilon_{axial}} \tag{4.10}$$

When a body is compressed in one direction, it tends to elongate in the transverse direction. Conversely, when a body is elongated in one direction, it gets thinner in the other direction. The typical value is around 0.3.

A *shear modulus G* can be defined as the ratio of the shear stress $(\tau)$ and the shear strain $(\gamma)$

$$G = \frac{\tau_{xy}}{\gamma_{xy}} = \frac{E}{2(1+v)} \tag{4.11}$$

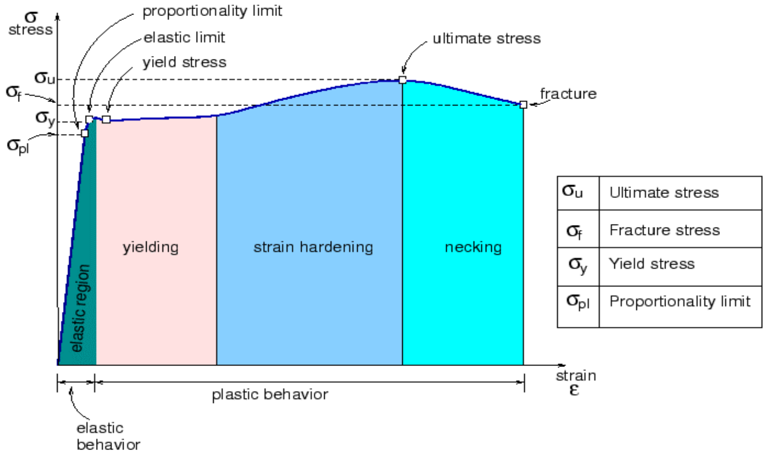


**Figure 4.2:** Stress-strain graph for a typical material

The proportionality between stress and strain is usually more complicated than suggested by Hooke's law.

## 4.2 Mechanical Structure of Cable

As shown in figure 4.5, the transmission line conductor is subjected to both tensile and bending stress due to the large amount of forces acting on the transmission line as seen in figure 4.3 (determined using OPERA 2D) which can cause cable movement and can also cause degradation of the superconductor which eventually leads to the magnetic field errors in the beam area (VOI), which we had observed in the previous chapter, the effect of conductor movement on the field quality.
The initial design considered have 4 set of cables which are supported by a GFRP structure with helium flow passage at the center and cables are placed on the arcs at each corner of the supoort structure

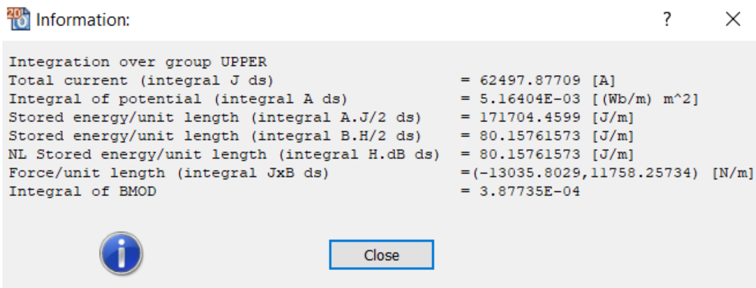


**Figure 4.3:** Total current and forces acting of transmission line [10].

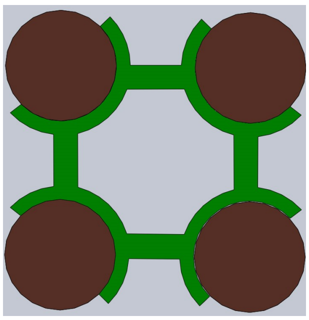

**Figure 4.4:** Transmission line cable structure.

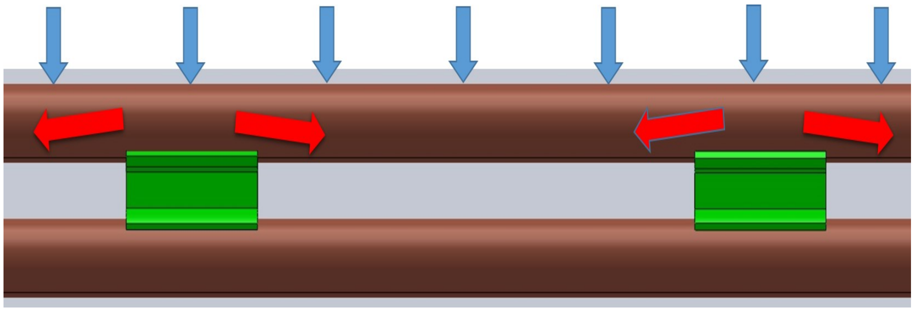

**Figure 4.5:** Forces acting on transmission line.

### 4.2.1 Static Structural Analysis

In order to reduce the overall cost of the magnet system with a structurally stable design, we need optimized spacing of the support structure without degrading the performance of the superconductor. FEM analysis using ANSYS can give us a good prediction of the stress and strain in the cable when forces are acting on the cable

In ANSYS static structural analysis, we had used the properties of OFHC copper as maximum load is expected to be handled by the copper tube and taking copper properties can give us more close results as compare of $MgB_2$.

As shown in figure 4.6 and figure 4.7 gives the maximum stress acting on the the cable when subjected to a resultant force of 17 kN/m which is acting on the superconductor and figure 4.8 and figure 4.9 shows the maximum strain acting on the cable.

For this study, we had considered two cases, one with a support at distance of 0.14 m and another case having support structure at the distance of 0.15 m. The maximum stress and strain that is acting on the 0.14 m is 455 MPa, 0.22% and in 0.15 m is around 518 MPa, 0.4% respectively. Here we are limiting the maximum length with a strain limit of 0.4%

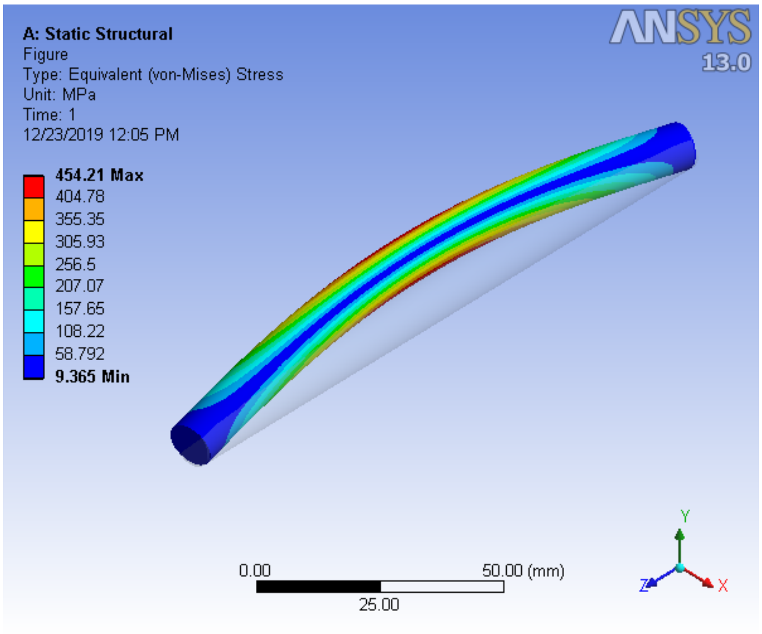


**Figure 4.6:** Stress distribution in 140 mm length cable.

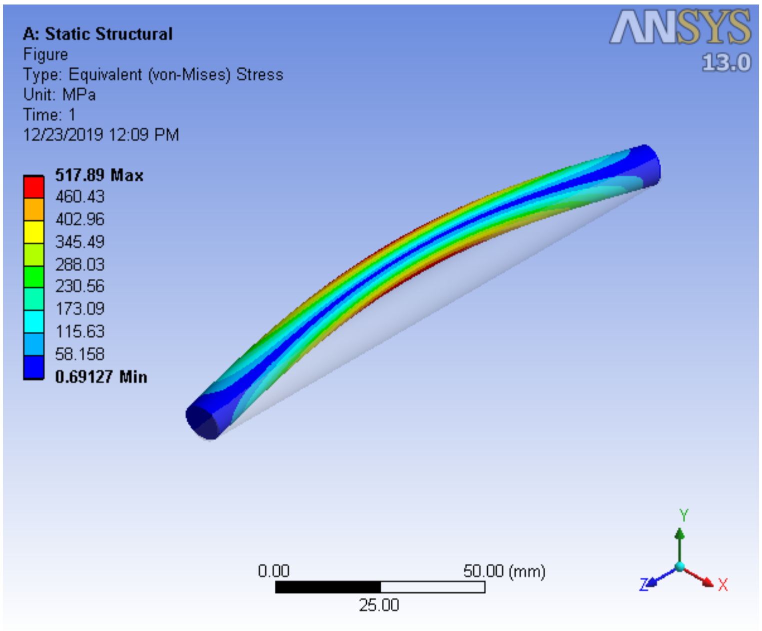


**Figure 4.7:** Stress distribution in 150 mm length cable.

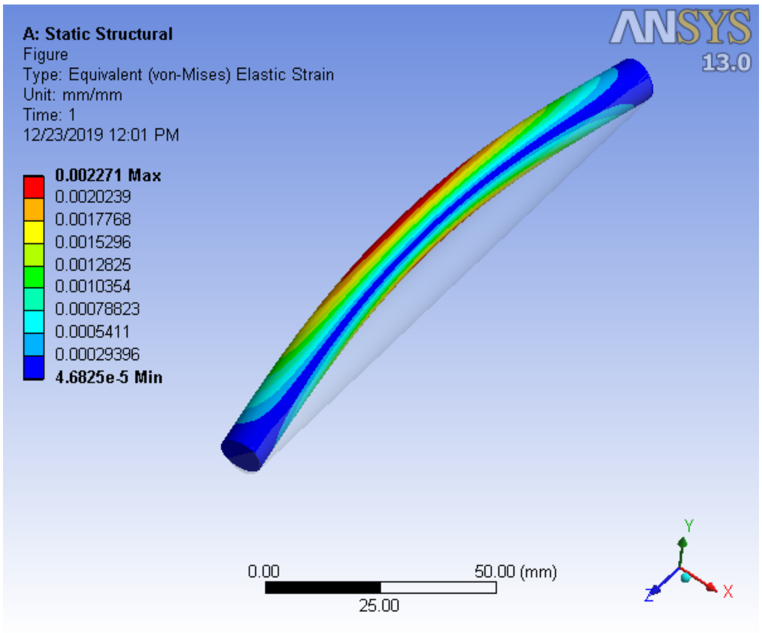


**Figure 4.8:** Strain distribution in 140 mm length cable.

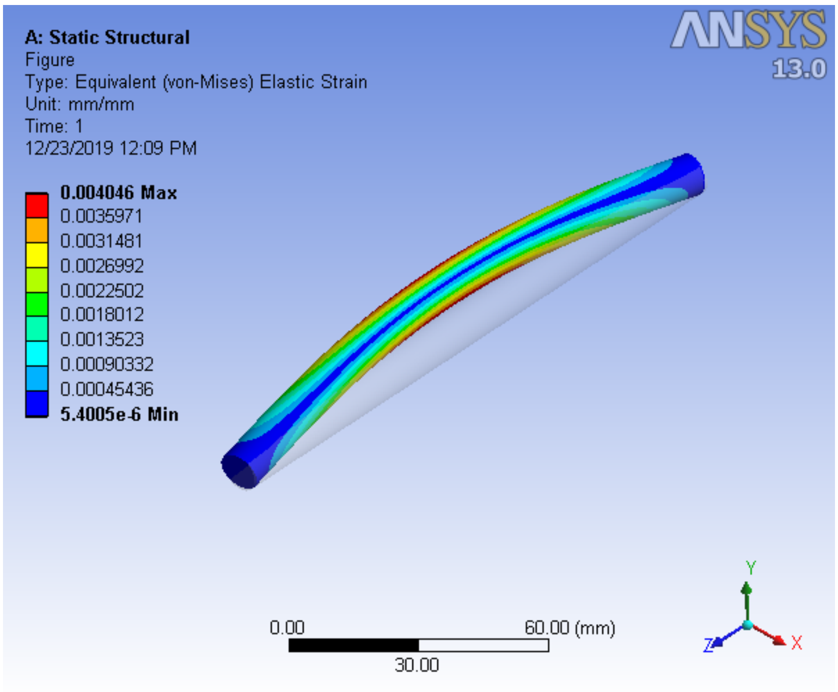


**Figure 4.9:** Strain distribution in 150 mm length cable.

## 4.3 Mechanical and electrical stability of MgB$_2$ Wires

As shown in previous section, when the support structures are places at a distance of 0.15 m, the maximum strain induced in the cable is around 0.4%. In order to check whether the MgB$_2$ sample wire can withstand the strain of 0.4% without degrading the performance we need to check the electromechanical properties of the MgB$_2$ sample wires.

In this section, we present a study of electrical and mechanical properties of the MgB$_2$ wire produced by three manufactures namely, **Hitachi**, **HyperTech**, and **Columbus**. We demonstrate that the working temperature have a large impact on the mechanical strength of the MgB$_2$ conductor, it gives the allowable strain that can be applied on the conductor during the fabrication of the cable. We also study the effect of the external magnetic field and stress that the conductor can handle while operation.

| | Hitachi | HyperTech | Columbus |
|---|---|---|---|
| Outer Diameter | 1.5 | - | 1 |
| Width (mm) | - | 1 | - |
| Thickness (mm) | - | 1.5 | - |
| No. of Filament | 10 | 18 | 37 |
| Cu stabilization | Internal | Internal | External |

**Table 4.1:** Geometrical characteristic of MgB$_2$ conductors

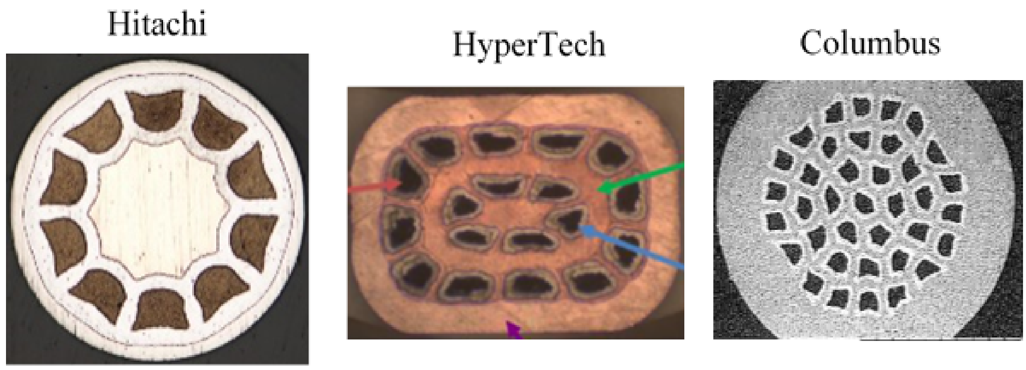


**Figure 4.10:** Cross-section view of Hitachi, HyperTech and Columbus sample wires

| | Hitachi | HyperTech | Columbus |
|---|---|---|---|
| $MgB_2$ | 24% | 10% | - |
| Copper | 21% | 21% | - |
| Iron | 40% | - | - |
| Monel | 15% | 39% | - |
| Niobium | - | 24% | - |
| Nickel | - | - | - |
| Tin-silver | - | - | - |

**Table 4.2:** Composition of the investigated $MgB_2$ conductors

### 4.3.1 Investigating $MgB_2$ Conductor

***Hitachi Wire:***

$MgB_2$ sample wire fabricated by Hitachi Ltd. uses the powder-in-tube **(PIT)** method and in situ process, consisting of magnesium and boron powder with a purity of 99.8% and 98.5% respectively, carbon as a dopant material was added with coronene $(C_{24}H_{12})$ [2].The sample wire composition used in this study as listed in *table 4.1*, and *table 4.2*. and cross-sectional view as shown in *figure 4.10*.The powdered Mg and B were packed in the iron tubes, which acts as a barrier for chemical diffusion [2]. The 1.5 mm diameter wire consisting of 10 $MgB_2$ filaments (Wire multi), each of diameter 36 microns and twist pitch of 200 mm, was selected for the characterization. Sample wire was annealed at 600C for 12 hr in vacuum before the test *figure C.1*.

### 4.3.2 Tensile test at RT and 77K

The Hitachi wire stress-strain (S-S) measurement at RT and 77 K was performed using a commercial tensile testing machine, with a load capacity of 5 kN (TCM-500). Two strain gauges (KYOWA SKF-27817) mounted at the center of 100 mm long sample wire, and a similar dummy sample was connected and placed near the test sample. To minimize strain gauge error, nearly, the entire surface of the strain gauge was glued to the sample wire and cured in the oven for 5 hrs *figure C.2*. Furthermore, for determining the position dependency of the S-S curve, two extensometers of gauge length 25 mm are connected with strain gauges [3]. Stress-Strain (S-S) measurement was performed on several samples during loading and unloading to check the reproducibility.

The stress-strain (S-S) behavior of Hitachi sample at RT, 77 K, and 4.2 K is shown in *figure 4.12*, the stress flattening starting at higher strain when tested at low temperature. The reason for such behavior is not sure, but there might be one possibility. At the lower temperature (4.2 K-77 K), due to higher ther-

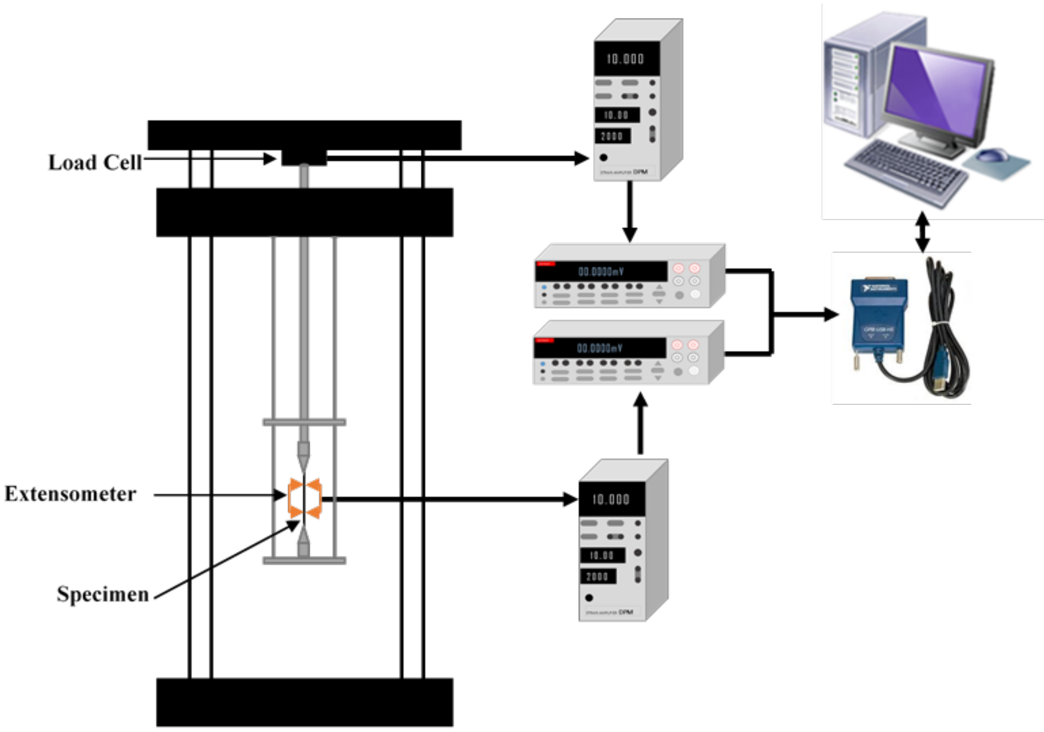


**Figure 4.11:** Schematic of tensile test setup at RT and 77 K

mal expansion of overall wire composition, $MgB_2$ filament may be subjected to higher compressive thermal residual strain, as reported in previous studies [6–8]. Strain applied at a lower temperature (4.2 K) shows a higher tolerance, compared to the 77 K, and RT under no external field, which gives $MgB_2$ more stability when operating in a liquid or gas helium environment. Additionally, extensometers were used for the S-S measurement on the tensile testing machine with the strain gauges. Both results show similar strain as there is no rise in the stress once the strain reaches 0.15% at RT and 0.39% at 77 K, whereas, the extensometer shows a rapid rise in strain once substantial filament damage occurs near the gripping section, which is the most vulnerable part. Deformation starts from the gripping/ soldered section, which was not detected by the strain gauges mounted at the center of the sample and they only show a maximum strain of 0.4%.

### 4.3.3 Tensile Test at 4.2 K and $I_c$ Measurement

S-S and $I_c$ measurement of Hitachi, HyperTech and Columbus was performed at 4.2 K using a customized test probe equipped with a 3 kN load cell, and HTS current leads to supply a maximum current up to 1 kA. For the test at 4.2 K, a 46

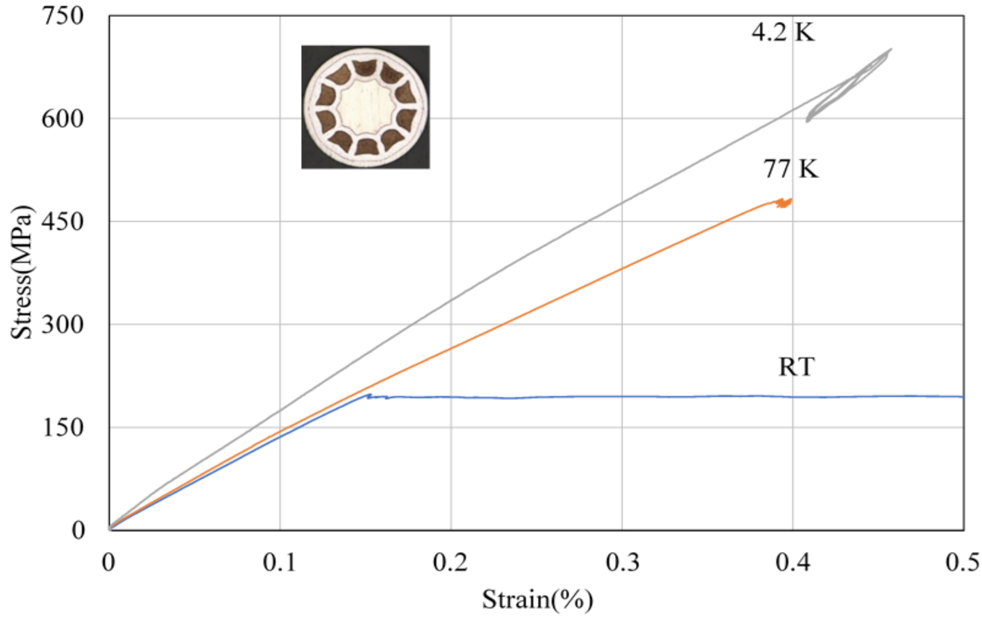


**Figure 4.12:** Stress-strain curve at variable temperature

mm - 47 mm sample wire was soldered on copper blocks of 7 mm each, two strain gauges were glued at the center of the sample wire, and voltage taps were placed at 5 mm from the sample center. Copper blocks are fixed on the test probe which can apply strain and current simultaneously. The critical current was measured using the four-probe method at 4.2 K and 10 T, with the criterion of the electric field fixed at 1 $\mu V/cm$ [2].

### 4.3.4 Field dependence on critical current $(I_c)$

***H*itachi wire:**

The critical current $(I_c)$ was measured at 4.2 K under no load condition, as a function of the applied external field. $I_c$ measurement was performed on 4 samples with a change in the external magnetic field between 7 T to 10 T, and the results obtained are 320 $\pm$30 A and 60 $\pm$5 A, respectively. The $I_c$-B measurement was limited to 7 T due to the shunt resistance of 500 A - 50 mV which allows a maximum current of 500 A, as seen in *figure 4.15* from the above results, it can be expected that $I_c$ may exceed 500 A at 6 T.

***H*yperTech wire:**

$I_c$ measurement was performed on 2 samples with a change in the external

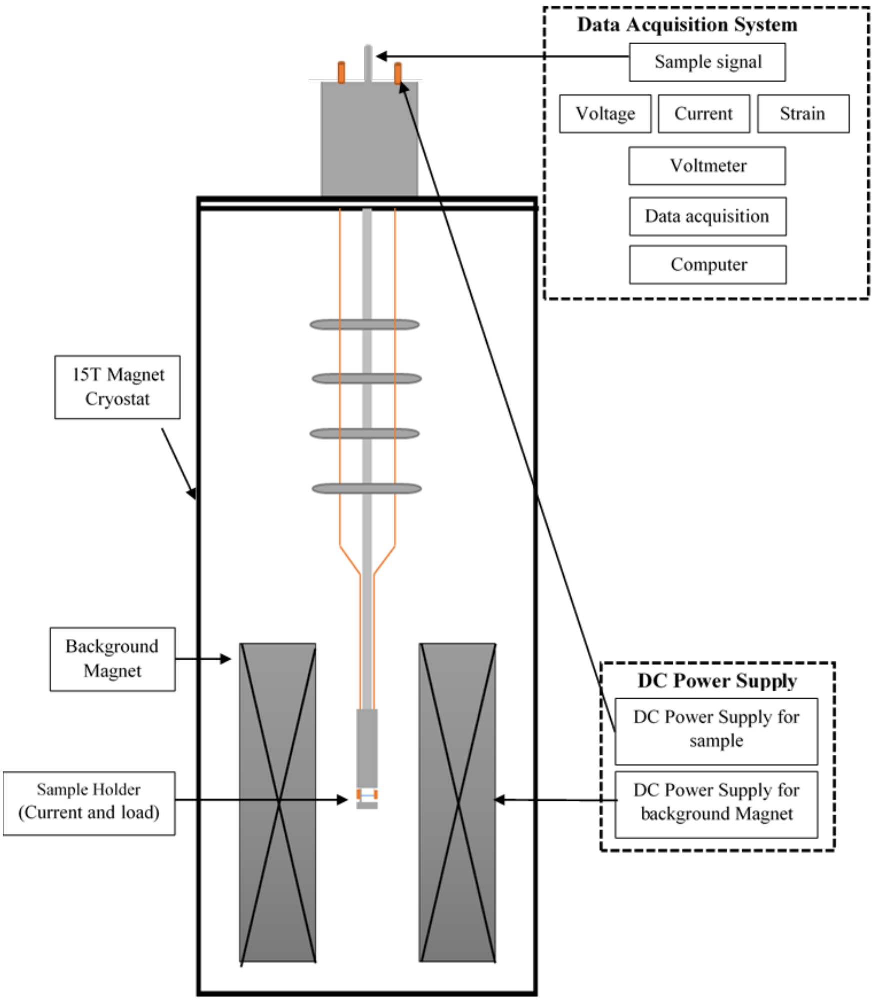


**Figure 4.13:** 4.2 K test setup

magnetic field between 3 T to 10 T, and the results obtained are 68 $\pm$10 A and 10 $\pm$5 A, respectively. As seen in *figure 4.16* both samples shows a large variation in the current which is not a desirable result.

***C*olumbus wire:**

$I_c$ measurement was performed on 2 columbus investigating samples with a change in the external magnetic field between 3 T to 10 T, as seen in *figure 4.17* , the results obtained are 116 $\pm$10 A and below 1 A, respectively and both the test show a slight variation which is desirable in $MgB_2$ conductor.

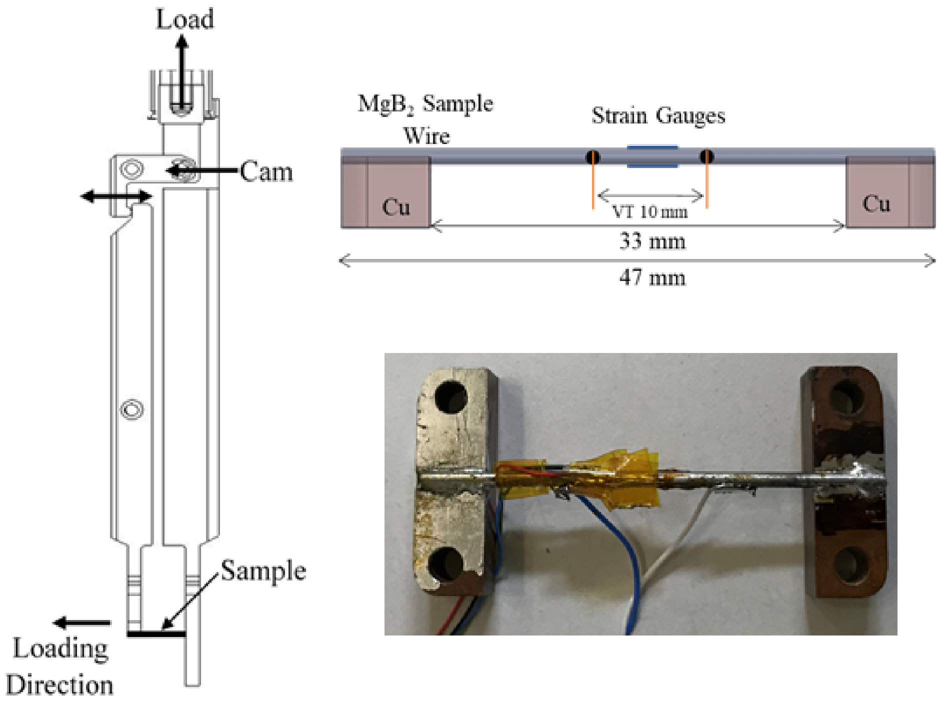


**Figure 4.14:** Schematic of direction of applied load and investigating sample

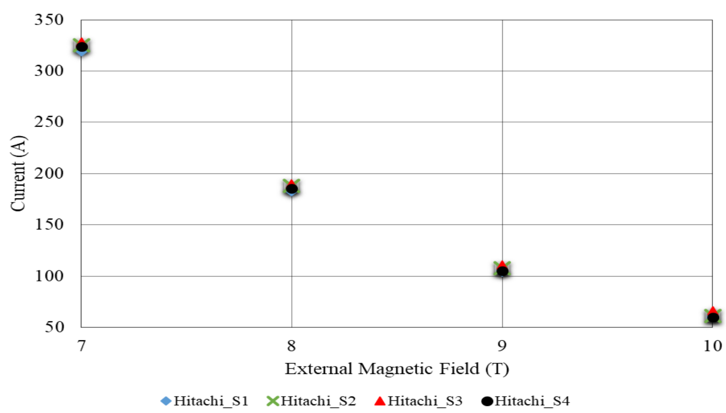


**Figure 4.15:** $I_c$ as a function magnetic field for Hitach $MgB_2$ wire at 4.2 K

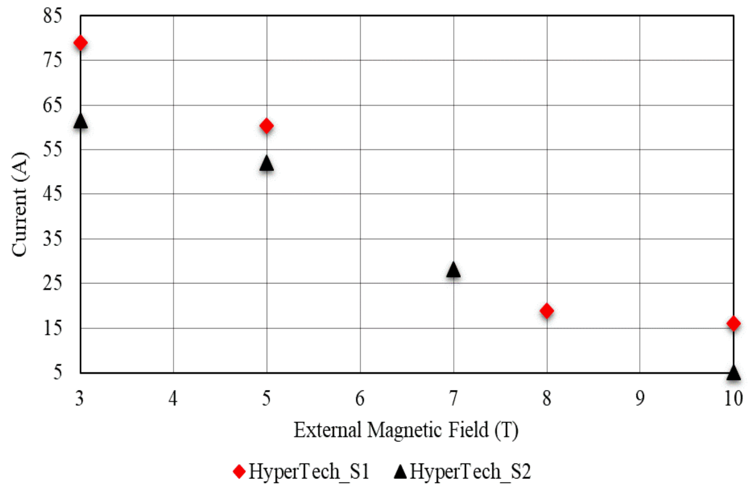


**Figure 4.16:** $I_c$ as a function magnetic field for HyperTech $MgB_2$ wire at 4.2 K

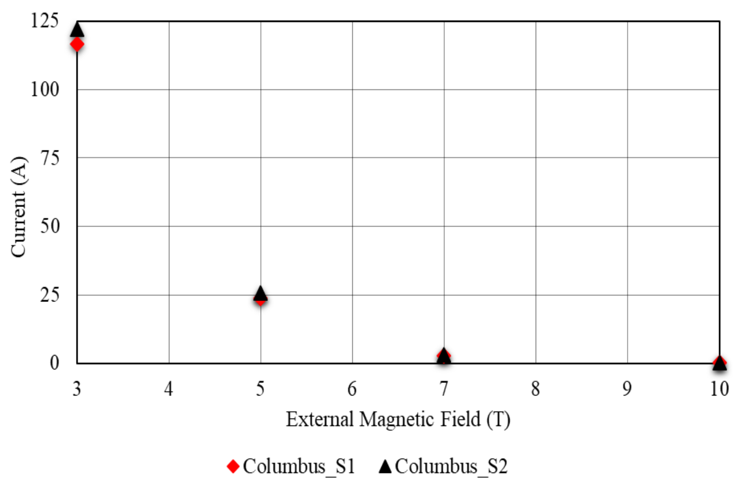


**Figure 4.17:** $I_c$ as a function magnetic field for Columbus $MgB_2$ wire at 4.2 K

### 4.3.5 Tensile Test and $I_c$ degradation by tensile strain

***Hitachi Wire***

In order to determine the threshold value at which $I_c$ starts to decrease, four short samples of 46 mm - 47 mm were tested with similar load conditions and the strain values were checked, at which a sharp decrease in the $I_c$ occurs, which was considered as the irreversible filament degradation. Under the external magnetic field of 10 T at 4.2 K, the uni-axial tensile strain was applied on all the samples. $I_c$/$I_{c0}$ ($I_{c0}$ being the critical current at 0% external strain) was plotted against the applied external strain figure 4.18. $I_{c0}$ of 4 samples are between 59 A and 61 A. The variation in $I_{c0}$ can be expected due to the in-homogeneity in the wire [2]. A linear rise in the $I_c$ was observed under an applied stress of about 0.4% on all samples. Due to the in-homogeneity of the $MgB_2$, we have observed that some samples shows a rapid degradation of $I_c$ as compared to the other samples. Above 0.4% strain, sample 2 and 3 shows an increase in the $I_c$ with a slight reduction in normalized value. A possible reason for such behavior can be due to partial breakage of the filament, and current can still flow until a significant breakage of the filament occurs. We had not observed any signal noise in the I-V measurement around 0.4% strain, which can indicate a significant filament breakage [4, 5]. as show in above figure 4.19 , it shows that S-S curves at 4.2 K, under 0 T and 10 T magnetic field, agree well in the strain range of 0% to 0.4%. Strain applied at 0 T is continuous without $I_c$ measurement, whereas at 10 T the strain was applied in incremental steps of 0.02% and $I_c$ was measured with each increment. At 0 T, $\epsilon_{max}$ is around 0.46% with a visible necking near gripping section. In the case of 10 T field,$\epsilon_{max}$ varies between 0.4-0.45% with degradation in $I_c$ and no visible necking in this range. Figure 4.20 shows the $I_c$ at 20 K under external field measured by Hitachi shows critical current around 2600 A. As the transmission line magnet is expected to be operating at 10 K, we are expecting a sufficient safety margin as at 20 K also the critical current is quite high and fulfill the requirements.

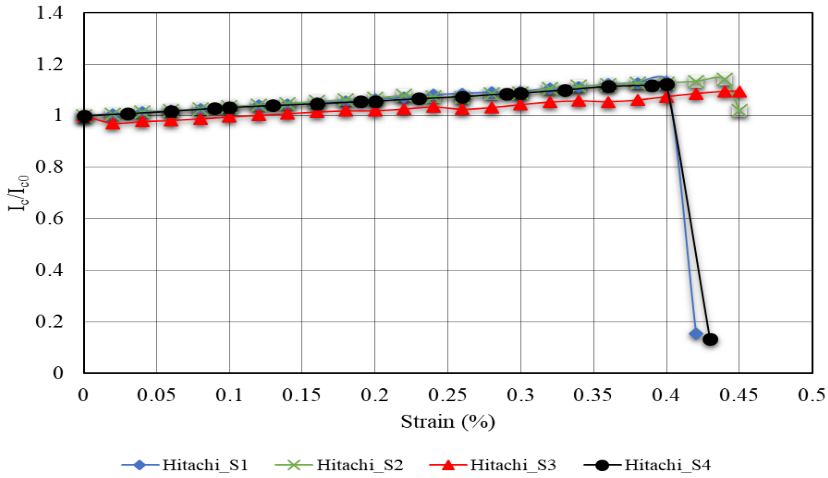


**Figure 4.18:** $I_c/I_{c0}$ dependence on strain at 4.2 K under external magnetic field.

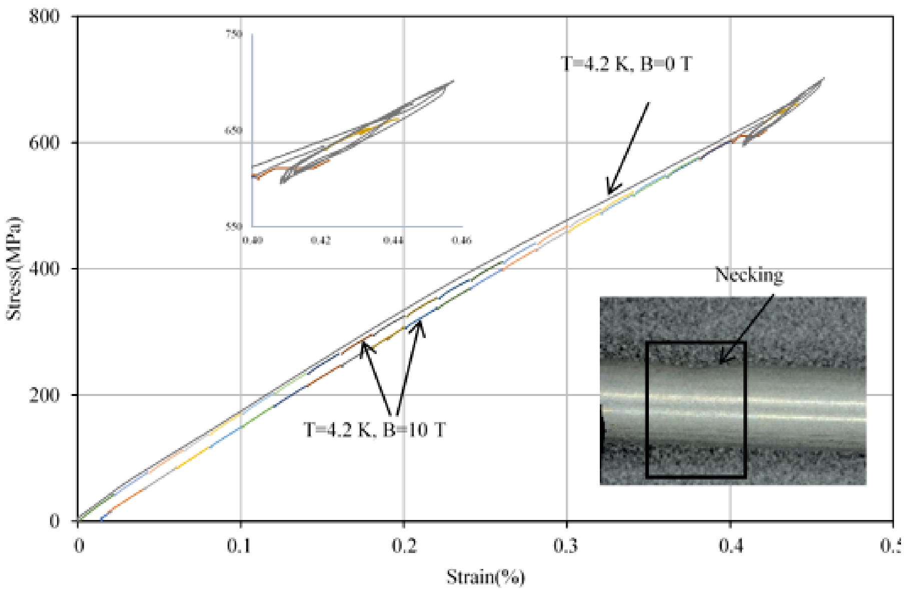


**Figure 4.19:** S-S curves at 4.2 K, under 0 T and 10 T magnetic field.

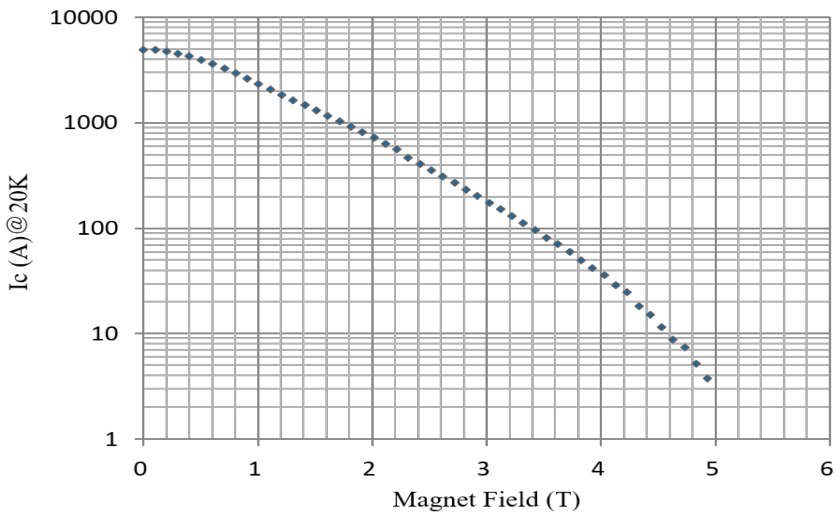


**Figure 4.20:** Critical current at 20 K under variable external field [Hitachi data]

## 4.4 Protection of superconducting magnets

### 4.4.1 Introduction

Circuits with superconducting magnets must have the same over-current and voltage-to-ground protection systems that are required for conventional magnet circuits. In addition, these circuits must have a quench protection system to protect the magnets when they lose their superconducting properties.

In superconductors, copper matrix stabilizes the cable and provide an alternative current path for a short time when the superconductor quenches and leaves its superconducting state so consideration of copper in the magnet quench protection system is an important thing and properties of copper need to be taken into consideration

### 4.4.2 Quenching

***Heating of the initiating spot (MIITs)***

A magnet conducting current in superconducting mode at cryogenic temperatures can suddenly lose its superconductive state, usually beginning at a particular spot in the magnet cable, when something causes the temperature at that spot to rise above the critical temperature. Once the initiating spot quenches, the heat generated from the resistance typically keeps it in the quenched state, and the quenched area spreads to nearby areas at a speed known as the 'quench velocity'.

Whenever a magnet quenches, the initiating spot starts to heat and is normally the place with highest temperature in the quenching magnet. Restraining this temperature below a damaging level (450K) is one of the most critical parameter in protecting the quenched magnet. In order to predict the quench temperature rise of a conductor carrying a current, adiabatic one-dimensional approximation is used. A simple heat balance equation given by:

$$\frac{I^2(t)\rho(T)}{A_{cu}}dt = AC_T dT \tag{4.12}$$

Rearranging and integrating above equations gives

$$\int_0^t I^2 dt = A_{cu}A\int_{T_b}^{T}\frac{C(T)}{\rho(T)}dT \tag{4.13}$$

The term on the left hand side is a time integral over the square of the current, this integral is called the miits limit of the cable usually this integral is in millions of amp squared seconds hence termed as MIITs ($10^6 A^2 - s$). To simplify the problem, it is assumed that the current decay is entirely controlled by the dump resistor. The current decays with a time constant of L/R where L is the inductance of the single magnet and R is the resistance of the dump resistor, which is connected to the single magnet.

The MIITs calculation is crucial for determining the two primary factors of the quench protection system:

– How quickly the current in the magnet must be reduced once the quench is detected.

– How quickly a quenched must be detected once the initiating spot quenches.

### 4.4.3 MIITs Calculation

**MIITs(Strand)**

$$AA_{cu}\int_{T_b}^{T}(\frac{C_{cu}D_{cu}A_{cu}}{\rho_{cu}A}+\frac{C_{MgB_2}D_{MgB_2}A_{MgB_2}}{\rho_{cu}A} + \frac{C_{Fe}D_{Fe}A_{Fe}}{\rho_{cu}A}+\frac{C_{monel}D_{monel}A_{monel}}{\rho_{cu}A})dt \quad (4.14)$$

**MIITs (Cable 18:1 (SC:Cu))**

$$(18A_{cu}+A_{custrand})\int_{T_b}^{T}(\frac{C_{cu}D_{cu}(18A_{cu}+A_{custrand})}{\rho_{cu}}+\frac{C_{MgB_2}D_{MgB_2}18A_{MgB_2}}{\rho_{cu}} + \frac{C_{Fe}D_{Fe}18A_{Fe}}{\rho_{cu}}+\frac{C_{monel}D_{monel}18A_{monel}}{\rho_{cu}})dt \quad (4.15)$$

A, $A_{cu}$, $A_{MgB_2}$, $A_{Fe}$=Cross sectional area of strand,copper ,$MgB_2$ and iron resp ($m^2$),

$C_{cu}$,$C_{MgB_2}$, $C_{Fe}$=specific heat of Copper,$MgB_2$,iron resp.(J/kgK),

$\rho_{cu}$=Resistivity of Copper ($\Omega$m ),

$C_{cu}$, $C_{MgB_2}$, $C_{Fe}$=specific heat of Copper,$MgB_2$,and Iron (J/kgK),

$D_{cu}$, $D_{MgB_2}$, $D_{Fe}$=Density of Copper,$MgB_2$,Iron(kg/$m^3$ )

Resistivity of copper is given by

$$\rho(n\Omega m) = \rho_0 + \rho_i + \rho_{i0} \tag{4.16}$$

$$\rho_0 = \frac{\rho(273K)}{RRR}, \qquad \rho_{i0} = \frac{P_7 \rho_i \rho_i}{\rho_i + \rho_0} \tag{4.17}$$

$$\rho_i = \frac{P_1 T^{P_2}}{1 + P_1 P_3 T^{(P_2+P_4)} \exp -(\frac{P_5}{T})^{P_6}} \tag{4.18}$$

$P_1$=1.17E$^{-17}$, $P_2$=4.49, $P_3$=3.84E$^{+10}$, $P_4$=1.14, $P_5$=50, $P_6$=6.428,

$P_7$=0.4531 RRR=300 , $\rho$(273K) =1.55E$^{-08}$

Specific heat of copper is calculated by [14]

$$C_{pcu} = 10^{a+b(\log_{10}T)+c(\log_{10}T)^2+d(\log_{10}T)^3+e(\log_{10}T)^4 +f(\log_{10}T)^5+g(\log_{10}T)^6+h(\log_{10}T)^7+i(\log_{10}T)^8} \tag{4.19}$$

the physical parameters are plotted in appendix section.

Initial cable composition (suggested by Hitachi as show in chapter 2) consist of 18 $MgB_2$ strand to 1 copper strand which is not sufficient to carry the required cable current., as shown in figure4.21.

The figure4.21 shows a relationship of MIITs as function of temperature and the time scale to show the maximum time for the reduction of current once a quench has been detected. For the present operating current of 80kA (6400 MIIT/s), the current in the quenching magnet much be reduced substantially in less than 1 second.

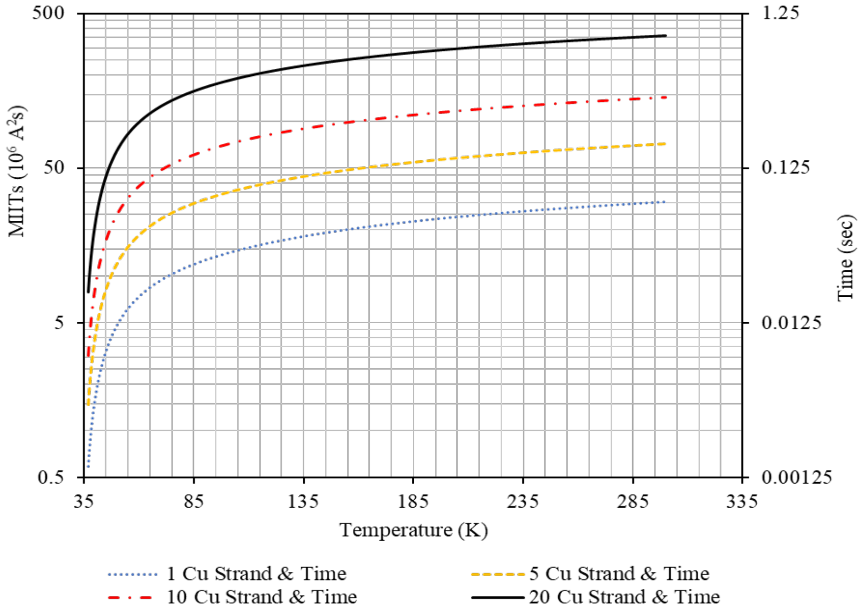


**Figure 4.21:** MIITs and time dependence of temperature based on the copper ratio in $MgB_2$ cable

## 4.5 Summary

In this chapter, we had performed FEA Analysis using ANSYS in order to check the optimal distance for placing the GFRP support structure in order to handle the forces acting on the cable and electro-mechanical characterization was performed to check the maximum limit of stress and strain that can be subjected on the conductor without degrading the performance of the superconductor.

For the optimized support distance we kept the threshold limit of strain to 0.4% and two cases are considered for check the range in which a support structure can be placed. In this study we performed analysis on support structures placed at 0.14 m and 0.15 m.

In order to test the conductor performance and degradation, test samples produced by the Hitachi, Columbus and HyperTech were tested at room temperature, 77 K and 4.2 K.
The electro-mechanical tests conducted are as follow:
(i)Stress and strain tests are performed at RT, 77 K and 4.2 K
(ii) Critical current measurement are performed on all the test samples at 4.2 K under variable magnetic field (load free) and variable strain (constant external field).

# Bibliography

[1] S.Timoshenko, Strength of Materials (D. Van Nostrand Company, New York, 1930)

[2] H. Tanaka et al.,"Tensile and bending stress tolerance on round MgB2 wire by insitu PIT process," IEEE Trans. Appl. Supercond., vol. 28, no. 4, Jun. 2018, Art. no. 8400605.

[3] P. Alknes et al., "Mechanical properties and strain-induced filament degradation of ex-situ and in-situ MgB2 wires," IEEE Trans. Appl. Supercond., vol. 26, no. 3, Apr. 2016, Art. no. 8401205.

[4] K. Yamamoto et al., "Mechanical and superconducting properties of PIT processed MgB2 wire after heat treatment," Supercond. Sci. Technol., vol. 16, no. 9, pp. 1052–1058, Sep. 2003.

[5] I. Hušek et al., "Tensile stress applied to NbTi, Nb3Sn, Bi-2223 and MgB2 composite superconductors at room temperature," Supercond. Sci. Technol., vol. 17, no. 12, pp. 1411–1414, Dec. 2004.

[6] J. W. Ekin, Experimental Techniques for Low-Temperature Measurements: Cryostat Design, Material Properties, and Superconductor CriticalCurrent Testing. New York, NY, USA: Oxford University Press, 2006.

[7] P. Kovác et al., "Dependence of the critical current in ex-situ multi and mono-filamentary MgB2/Fe wire on the axial tension and compression," Supercond. Sci. Technol., vol. 16, no. 5, pp. 600–607, Mar. 2003.

[8] J. J. Neumeier et al., "Negative thermal expansion of MgB2 in the superconducting state and anomalous behavior of the bulk Grüneisen function," Phys. Rev. B, vol. 72, Dec. 2005, Art. no. 220505.

[9] H. Pfeffer et al., "Protection of hardware: Powering systems (power converter, normal conducting, and superconducting magnets)," Joint Int. Accel. School: Beam Loss Accel. Protection, Newport Beach,

CA, USA, CERN Yellow Report CERN-2016-002, pp. 343–360, Nov. 2014.https://e-publishing.cern.ch/index.php/CYR/article/download/240/211

[10] Opera simulation software. Dassault Systèmes, 2018.

[11] R. Flora et al.,"Quench Development in Magnets made with Multi-filamentary NbTi Cable," IEEE Transactions on Magnetics, Vol. MAG-13, No. 1, (1977) http://ieeexplore.ieee.org/document/1059379/

[12] S. Russenschuck,"Field calculation for accelerator magnets."(Chapter 18-Quench Simulation)

**APPENDIX - B**

[13] Analytical formulas for current dynamics and peak temperature during a quench in MRI. "Medical Instrumentation, ISSN 2052-6962, Volume 2, Article 3" http://www.hoajonline.com/medicalinstrumentation/2052-6962/2/3

[14] NIST Cryogenics, Material Properties: OFHC Copper (UNS C10100/C10200) http://cryogenics.nist.gov/MPropsMAY/OFHC%20Copper/OFHC_Copper_rev.htm

[15] Review of ROXIE's Material Properties Database for Quench Simulation. https://espace.cern.ch/roxie/Documentation/Materials.pdf

[16] cryogenic-data-handbook. https://www.bnl.gov/magnets/Staff/Gupta/cryogenic-data-handbook/Section8.pdf

[17] Specific heat in the superconducting and normal state(2-300K,0-16 Teslas), and magnetic susceptibility of the 38-K superconductor MgB2: evidence for a multicomponent gap https://arxiv.org/ftp/cond-mat/papers/0103/0103181.pdf

[18] Properties of k-monal at low temperature.http://indico.cern.ch/event/194284/contributions/1472798/attachments/281498/393574/CAS_propmat_2013.pdf

[19] http://www.hightempmetals.com/techdata/hitempMonelK500data.php

# Chapter 5

# Results and Discussion

## 5.1 Optimization of Pole

As shown in chapter 2 the pole profile generated by numerical formula is lack of target field quality. In order order to get the target field in the VOI region, in chapter 3, we optimized the pole profile using singular value decomposition. The results of the optimization of pole profile using Singular Value Decomposition gave field components close to the target dipole, quadrupole and sextupole field of 1.15 T , -3.14 T/m and 17 T/m$^2$ . In order to validate the SVD optimization method, combined function profile generated by numerical formula was subjected to the SVD optimization to get the dipole pole profile as shown in figure 5.1 and the method showed satisfactory result in converging the hyperbolic profile into flat pole profile which give only dipole field components and all higher order components are of the order of $10^{-4}$ T.

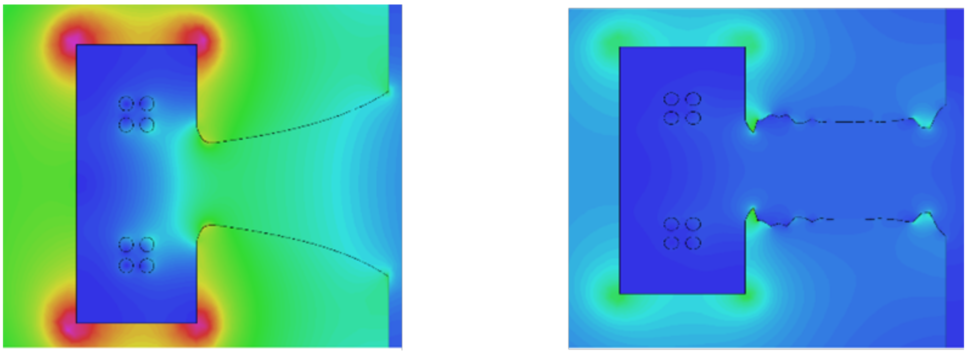

**Figure 5.1:** Convergence of pole profile from combined function (curved) to dipole (flat)

But one limitation we found in this method is generation of pole profile with complex geometry which can be commercially difficult to manufacture. In order to over come this issue one possible option that had adopted is to divide the shimming points into pair of 5 and take average of the shimming amplitude that is generated using eigen mode strength and use the average amplitude for getting the pole profile for the next iterative step.By improving and taking the above process into consideration, we were able to get a much smoother and commercially feasible shape.

## 5.2 Effects of conductor displacement

In accelerator systems field quality is key concern in order to keep the beam on the trajectory.As,the magnet is subjected to large amount of forces as well as faces thermal cycles which can induce movement in the coil/cable.In chapter 3 we had created a asymmetry in the coil by displacing the top conductor by 5 mm in X and Y from the symmetry condition, due to this displacement we found variation in the field components in the VOI region.

5 mm displacement in the conductor induced skew component of order higher than $10^{-4}$ T. This define the tolerance limit of less than 5 mm displacement in the conductor, under 5 mm we had not found any significant change in the field components and all the higher order component are under the specified field limit.

## 5.3 Mechanical support structure

In order to determine the stress and strain acting on the cable we used the ANSYS static structural analysis and applied the force of 17 kN/m which we found from OPERA 2D simulation over the length of the cable. In order to get the optimal gap for the GFRP support we kept the maximum strain limit of 0.4%. For a length of 0.15 m we found that the strain is 0.4% where as for 0.14 m the maximum strain is 0.22%.

Taking safety margin we can say that 0.14 m grap between two support structure can give a stable structural stability to the cable.

## 5.4 Electromechanical characterization of $MgB_2$ wire

As we found from the structural analysis stress of around 0.4% is acting on the superconducting cable, we need to determine the mechanical properties of the $MgB_2$ wire at variable temperature. In chapter 4 we had performed tensile test at RT, 77 K and 4.2 K.

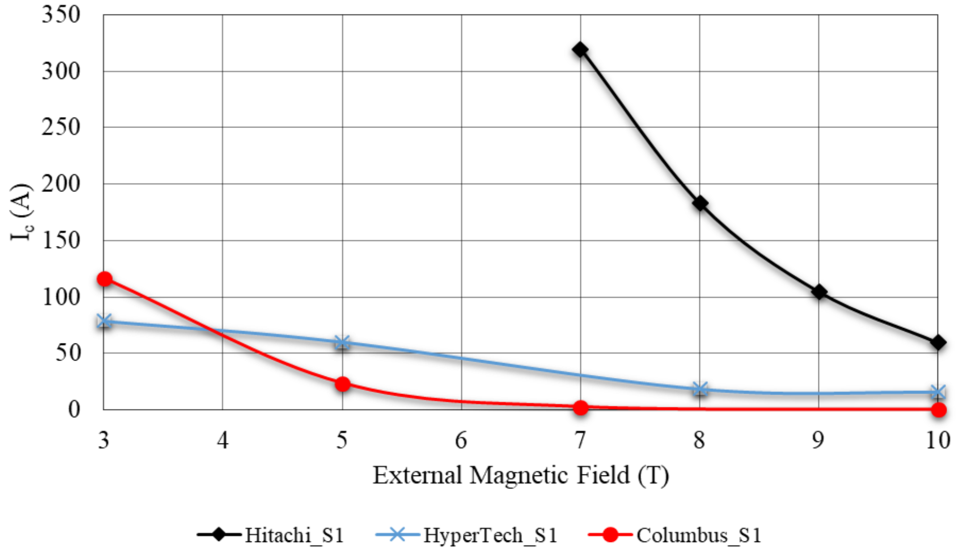


**Figure 5.2:** Comparison of $I_c$ as a function of external magnetic field in three $MgB_2$ wire with different composition

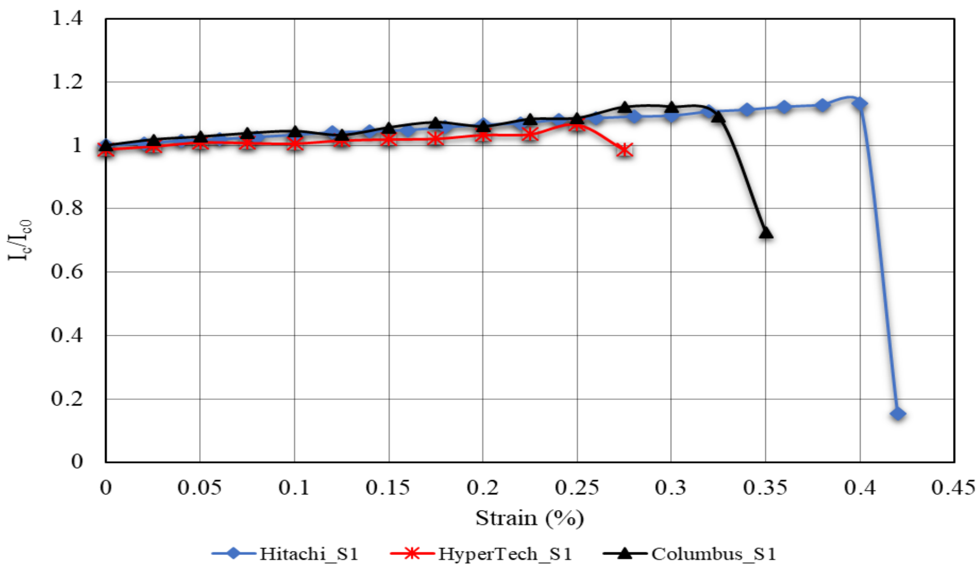


**Figure 5.3:** Comparison of $I_c$/ $I_{c0}$ as a function of applied strain in three $MgB_2$ wire with different composition

Figure 5.2 shows a large variation in the critical current of three investigated samples provided by Hitachi, HyperTech and Columbus with Hitachi wire having the highest critical current value ($I_c$) at high external field (minimum 7 T). For the transmission line magnet the external field is below 2 T, Hitachi sample was only investigated at minimum field of 7 T which is quite high as compare to the actual operational field, due to the limitation of test setup, investigation of Hitachi sample was not possible at low field.

On the other side, we had observed that the critical current of HyperTech and Columbus wire is quite low as compare to Hitachi with a resistive behavior seen in the I-V curve. In the present test setup the sample length is limited to less than 50 mm due to magnet cryostate bore which restricts the use of longer sample, resistive behavior in small was reported in other articles also. In order to reduce this, there is a need to increase the distance of voltage taps from the copper blocks on which sample is soldered.

Results of Hitachi and Columbus samples are reproduced with an expected variation suggested by manufacturer (Hitachi) of $\pm 7\%$ ,where as HyperTech samples showed a large deviation in lower external magnetic field.

Figure 5.3 the effects of applied strain on the critical current of the $MgB_2$ samples, we have observed that all the samples when tested at 4.2 K initially shows a rise in the critical current when strain is applied until the point of irreversible filament degradation, this type of behavior in $MgB_2$ can be due to thermal contraction happened at low temperature.

We have observed that in Hitachi and Columbus samples an increase in the current up to 10% - 12% depending on filament degradation where as the increase in HyperTech is less than 5% which we had seen in the investigated samples.

Electromechanical characterization of Hitachi $MgB_2$ satisfies the threshold limit of 0.4% strain limit, taking in account the safety factor, GFRP support at a distance of 0.14 m gives a sufficient safety margin with maximum stain acting of 0.22%.

# Chapter 6

# Conclusion

In this work we have presented the study of transmission line magnet design and $MgB_2$ superconductor as a possible candidate for the J-PARC upgrade program which is expected in near future. This superconductor is considered as one of the substitute of Nb-Ti in superconducting magnets due to high operating temperature and low cost.

## 6.1 Numerical Results

Superferric C-shaped combined function type magnet is studied due to compact size and comparatively easy design.
-The iron yoke is optimized for a combined function which is mainly subject to the multipole error in superferric magnets taking in account the a stable design.
-Singular value decomposition method is used to optimize the pole profile and the optimization technique showed good results.
-The effect of coil movement on the multipoles and field quality is studied to optimize the coil movement and tolerance for the magnet system.
-Based on the operating current and available space in the iron yoke the required amount of copper in the transmission line in order to handle the heat load in case of quench is estimated.

## 6.2 Experimental Results

The electromechanical behavior of $MgB_2$ wire is studied to check the possiblity for the transmission line magnet
-Three sample wires of Hitachi, HyperTech and columbus are investigated.
-Stress and strain behavior of $MgB_2$ wire at RT, 77K and 4.2K was examined.

-Critical current dependence on the external magnetic field and applied strain was examined in order to check the tolerance of the three sample wire with different compositions.
-In this study the results of Hitachi sample shows a good reproducibility with higher current carrying capacity in high external magnetic field and applied strain as compare with other two investigated samples.

## 6.3 Outlook

Further work will have to include:

-Performance of the cable with the composition mention in this study need to be done in order to check the actual current carry capacity of the cable after deformation due to winding.
-Mechanical design study of the complete transmission line with cryogenic system.

# Appendix

## A. Supplementary Information: Optimization by SVD

- Combined function to Dipole field profile convergence

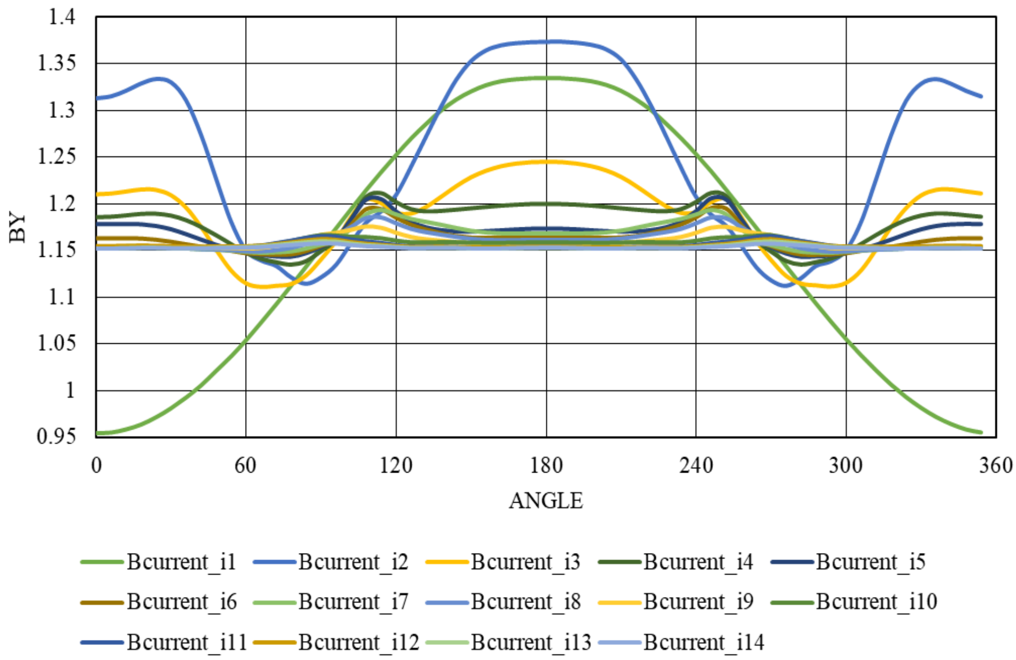


**Figure A.1:** $B_y$ variation with iterative steps

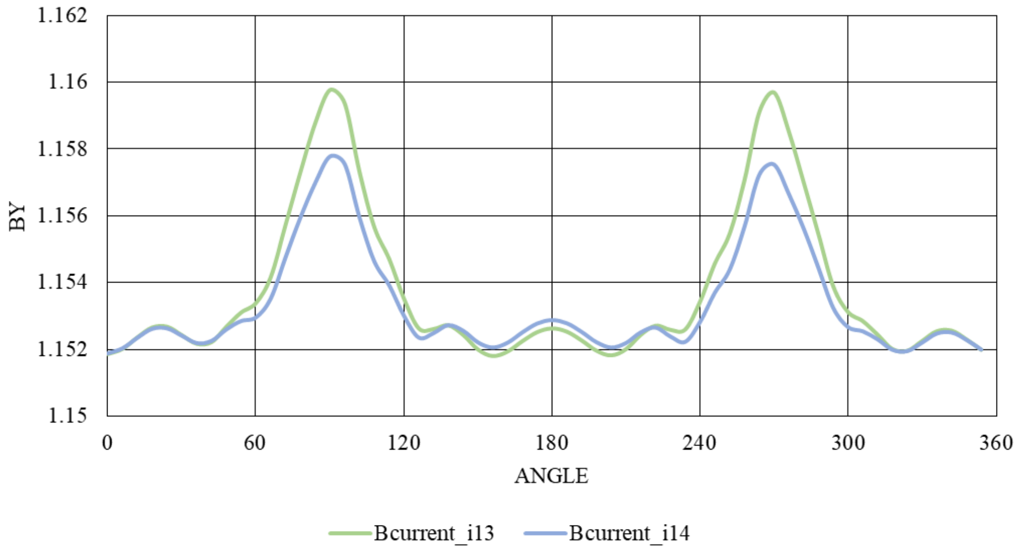


**Figure A.2:** Field after 14 iterations

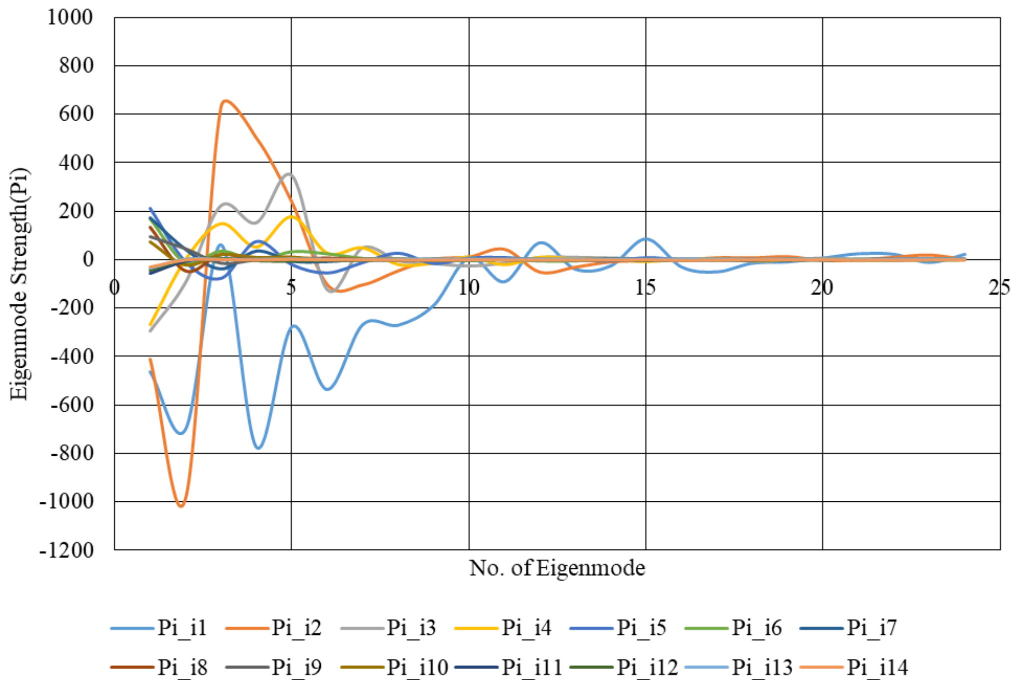


**Figure A.3:** Eigenmode strength as a function of number of eigen modes

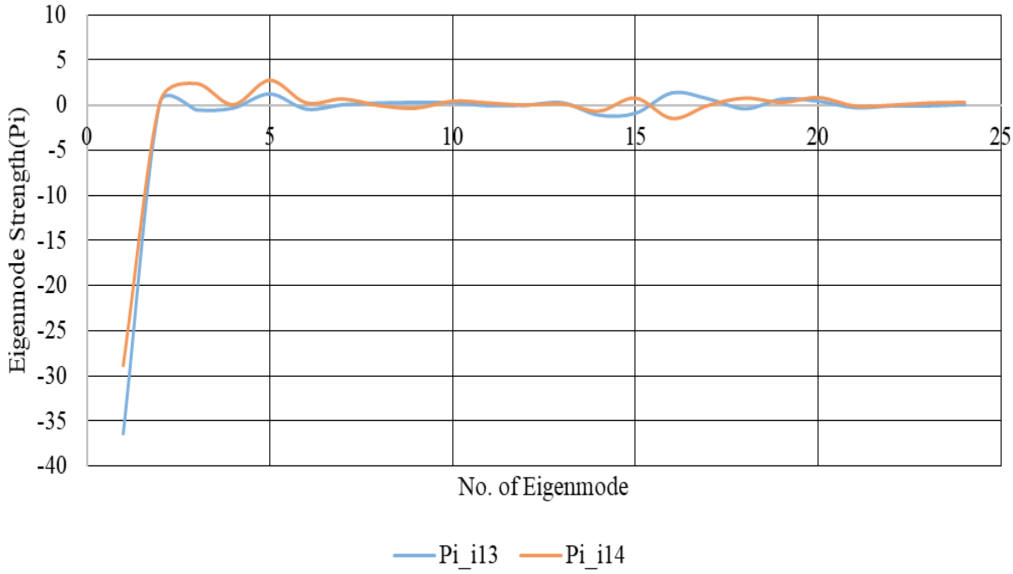


**Figure A.4:** Reduction in strength of higher eignmodes after several iteration

| n | Iteration1 | Iteration14 |
|---|---|---|
| 1 | 1.150936119 | 1.153443327 |
| 2 | -0.19436498 | -1.0901E-04 |
| 3 | -4.0034E-03 | -1.8461E-03 |
| 4 | 2.45783E-03 | -7.4647E-06 |
| 5 | -2.2374E-03 | 1.23243E-03 |

**Table A.1:** Reduction of Higher field components by SVD method

## B. Supplementary Information: MIITs calcualation data

- Specific Heat

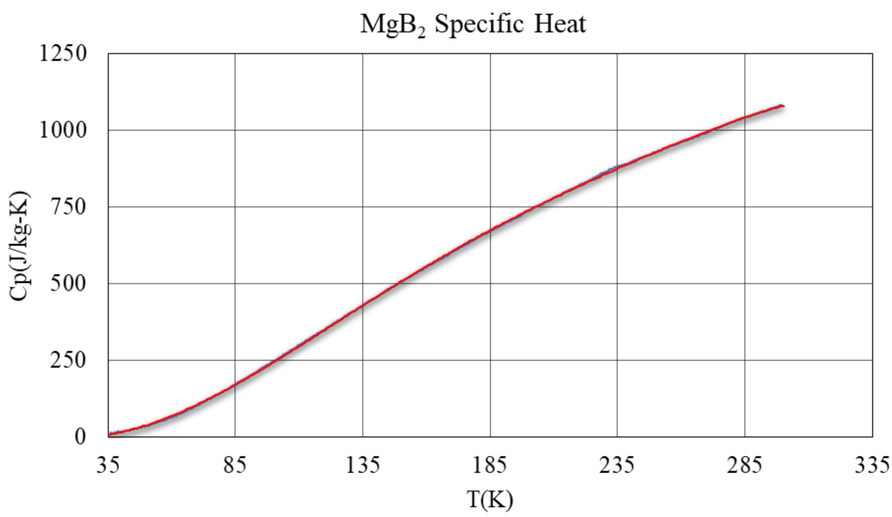


**Figure B.1:** Variation of specific heat of $MgB_2$ with temperature. [17]

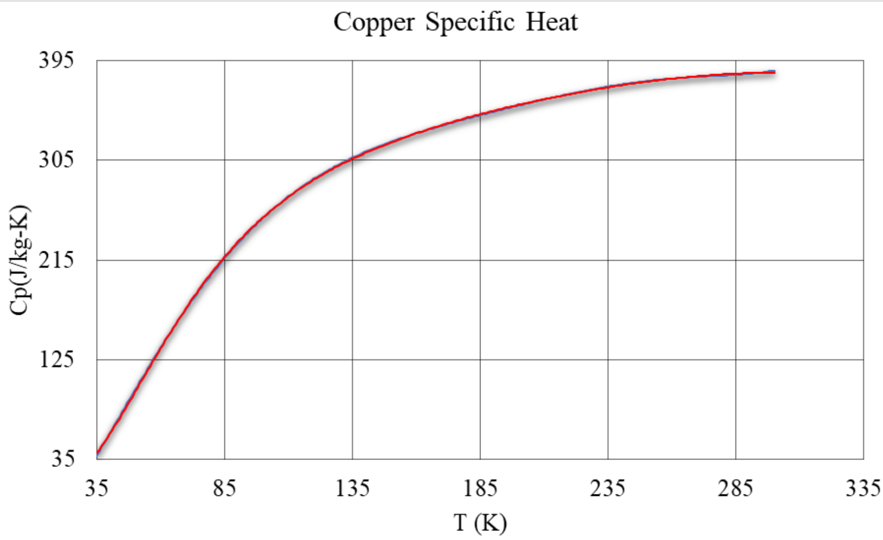


**Figure B.2:** Variation of specific heat of copper with temperature. [14]

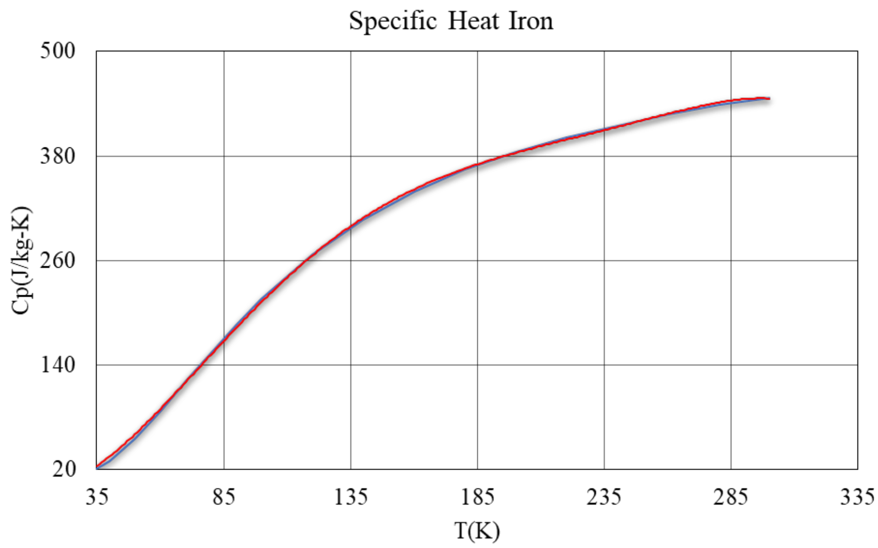


**Figure B.3:** Variation of specific heat of iron with temperature. [16]

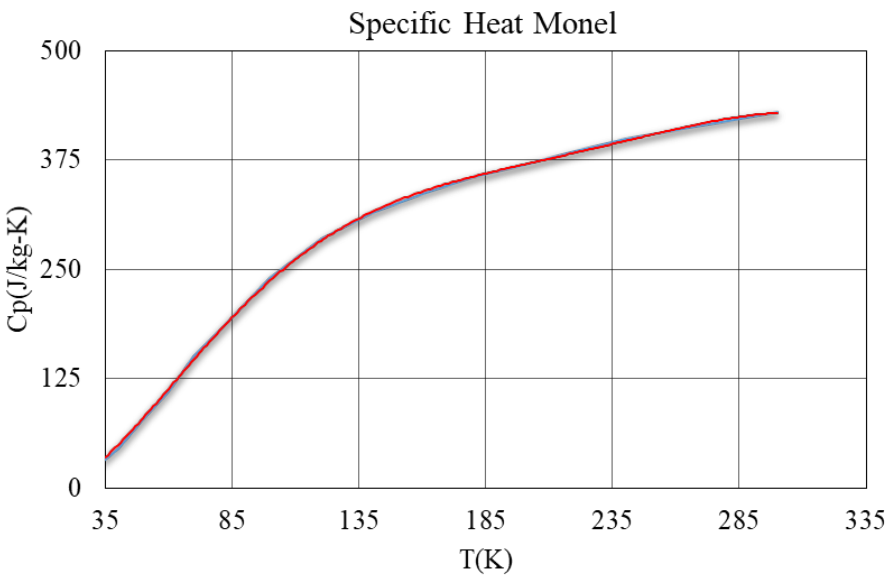


**Figure B.4:** Variation of specific heat of monel with temperature. [18, 19]

- Resistivity

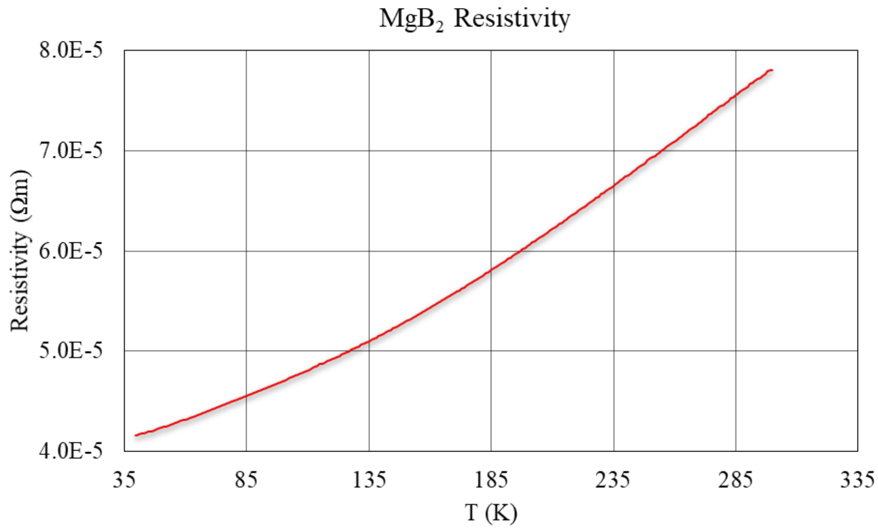


**Figure B.5:** Variation of resistivity of $MgB_2$ with temperature

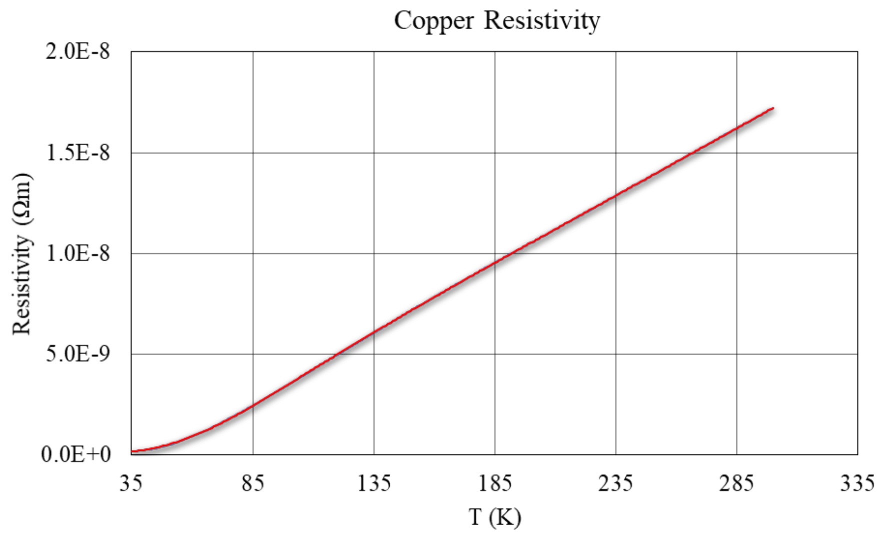


**Figure B.6:** Variation of resistivity of copper with temperature. [14]

## C. Supplementary Information: Sample preparation setup

- Test setup for RT and 77K


**Figure C.1:** Vacuum furnace for annealing sample wire

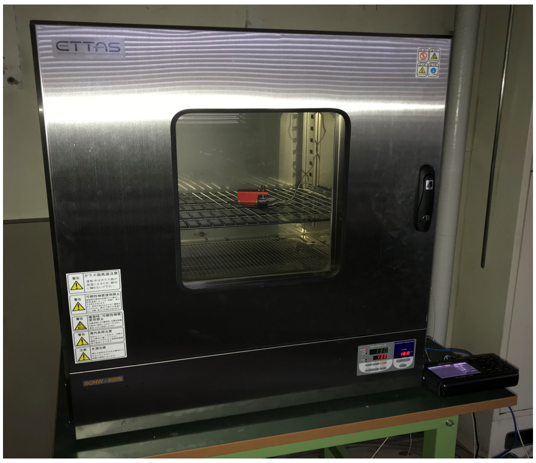


**Figure C.2:** Furnace for strain gauge bonding

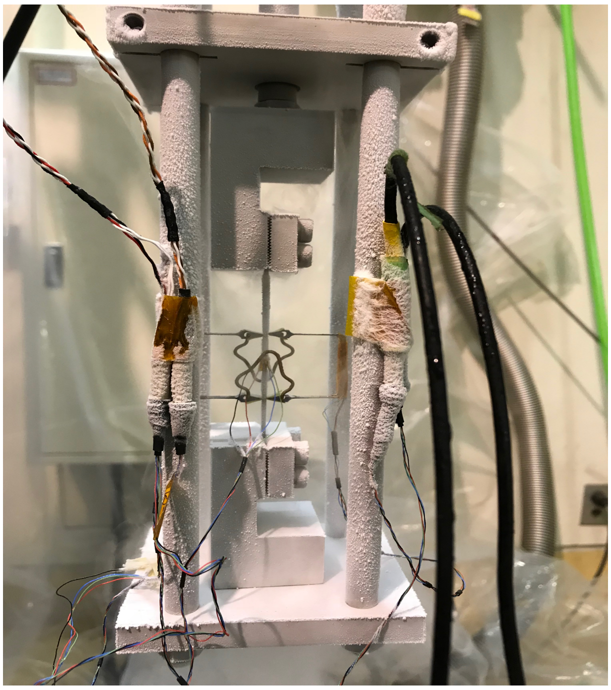

**Figure C.3:** RT and 77 K tensile test setup

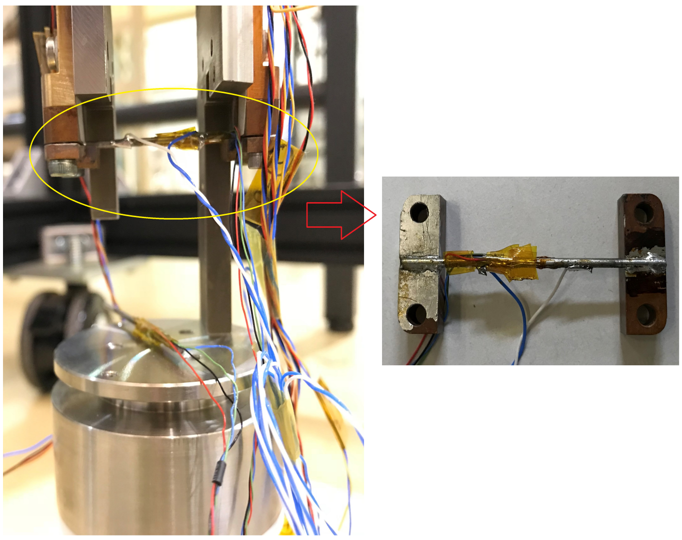

**Figure C.4:** 4.2 K test probe sample space

**Figure C.5:** 4.2 K test probe

## D. Supplementary Information: $MgB_2$ Characterization

- **Hitachi Sample wire**

- $I_c$ dependence due to external field

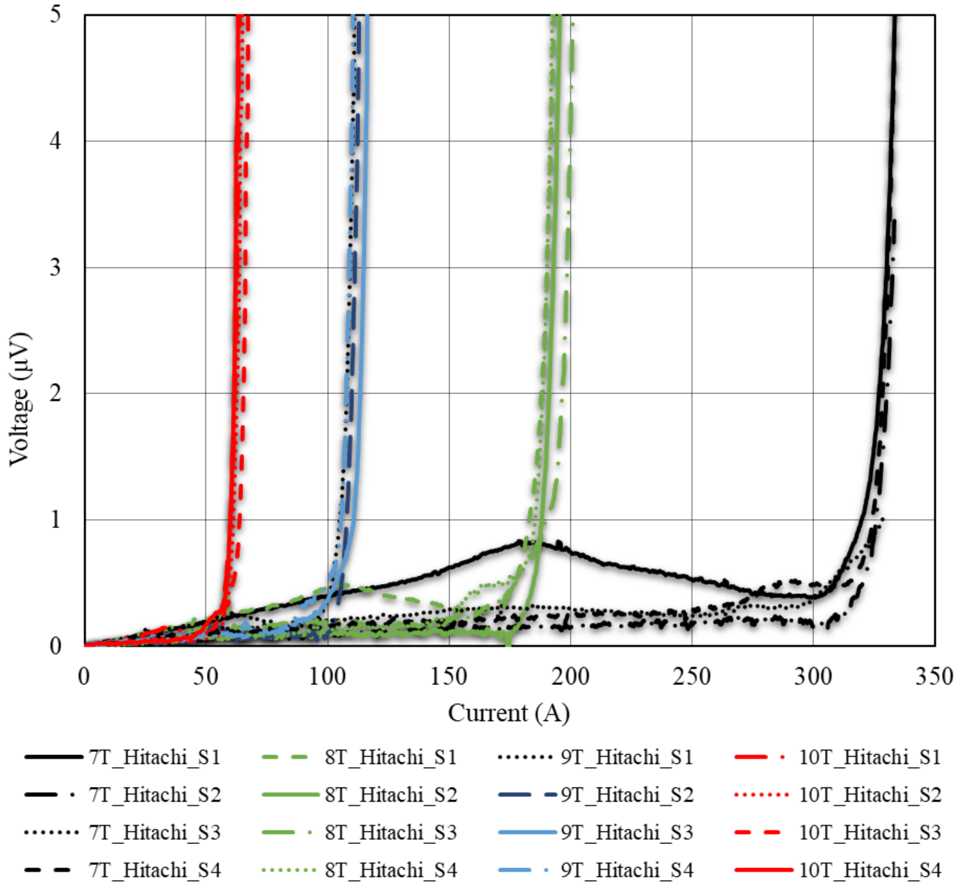


**Figure D.1:** Hitachi samples dependence of external magnetic field on critical current, strain = 0 %

figureD.2 shows a linear rise in the voltage, this resistive behavior was only observed in one test sample of Hitachi, one possible reason for this behavior is due to improper twisting of voltage tap wires and other signal wires. This issue was taken into consideration in further tests and further investigated samples produced by Hitachi has not shown such behavior.

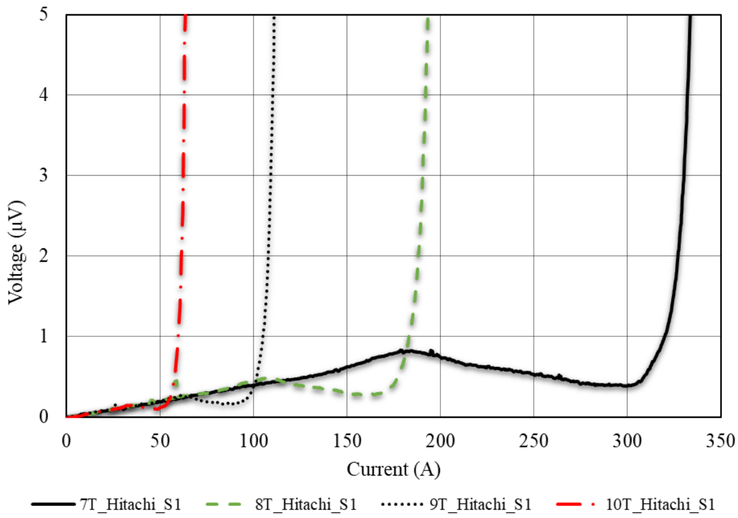


**Figure D.2:** Hitachi Sample 1 - I-V curve under variable field (7 T - 10 T) under 0 % strain

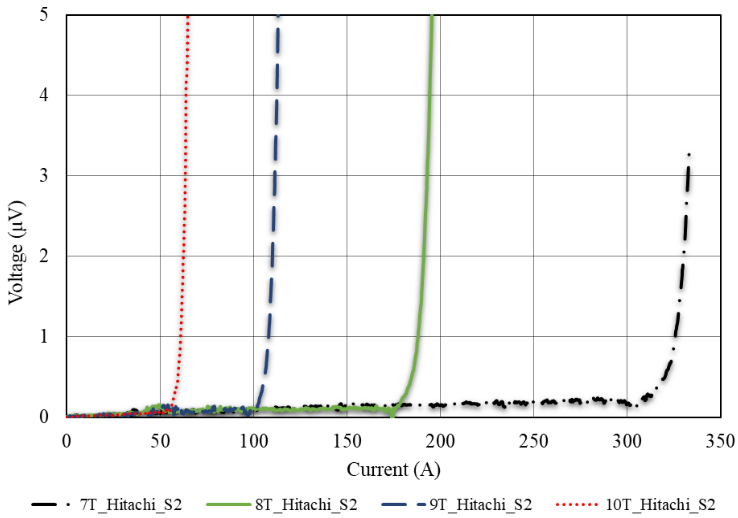


**Figure D.3:** Hitachi Sample 2 - I-V curve under variable field (7 T - 10 T) under 0 % strain

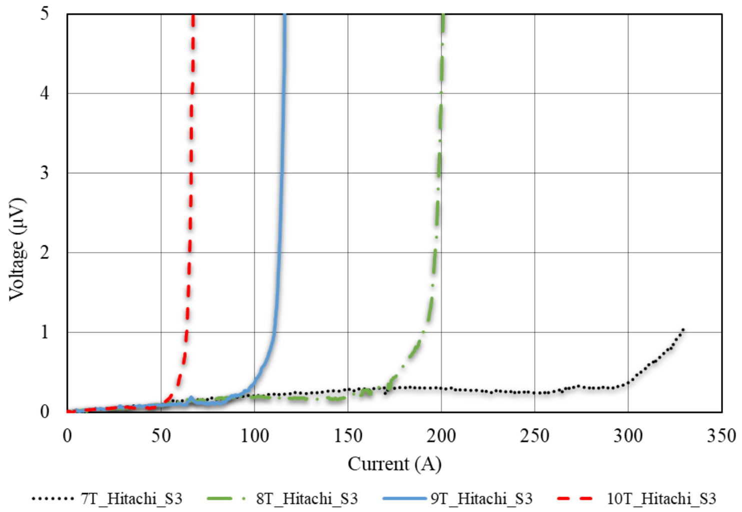


**Figure D.4:** Hitachi Sample 3 - I-V curve under variable field (7 T - 10 T) under 0 % strain

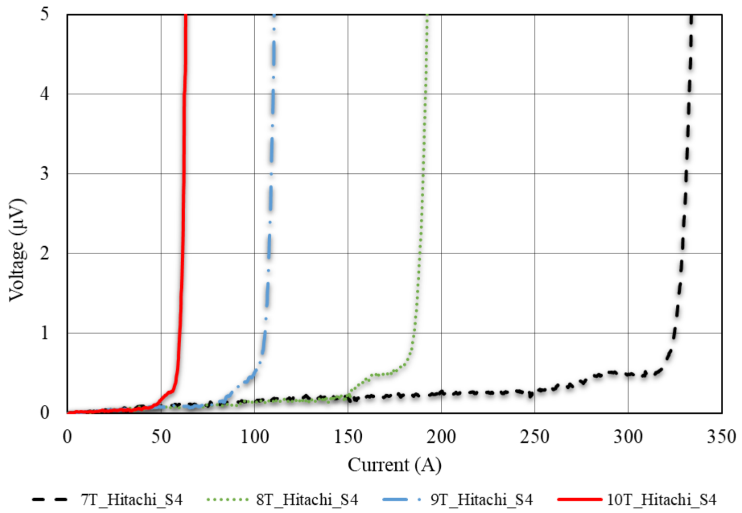


**Figure D.5:** Hitachi Sample 4 - I-V curve under variable field (7 T - 10 T) under 0 % strain

- **Columbus Sample wire**
- $I_c$ dependence due to external field

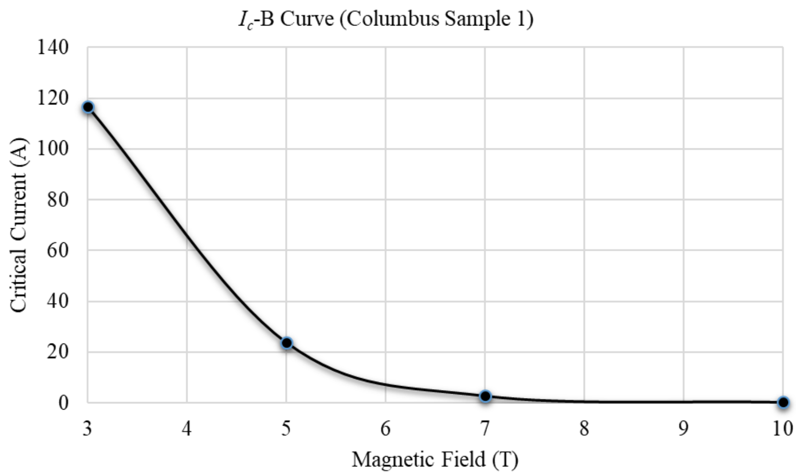


**Figure D.6:** Columbus sample 1- critical current as a function of external magnetic field

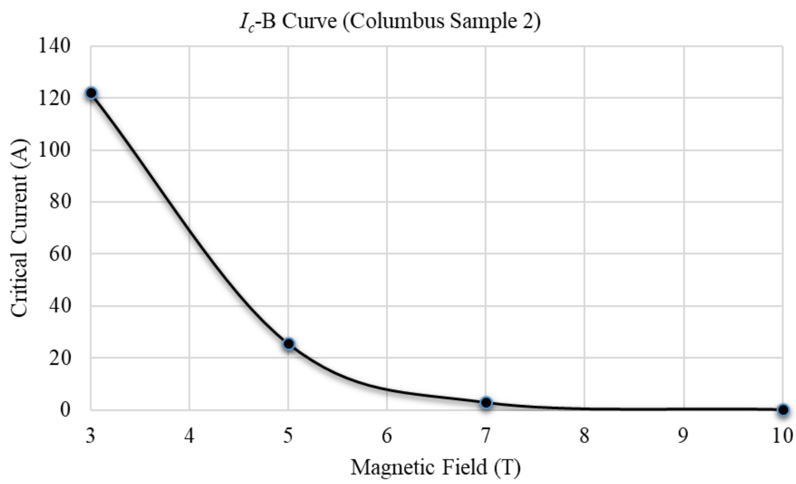


**Figure D.7:** Columbus sample 2- critical current as a function of external magnetic field

- I-V curve ; strain=0%; variable external field

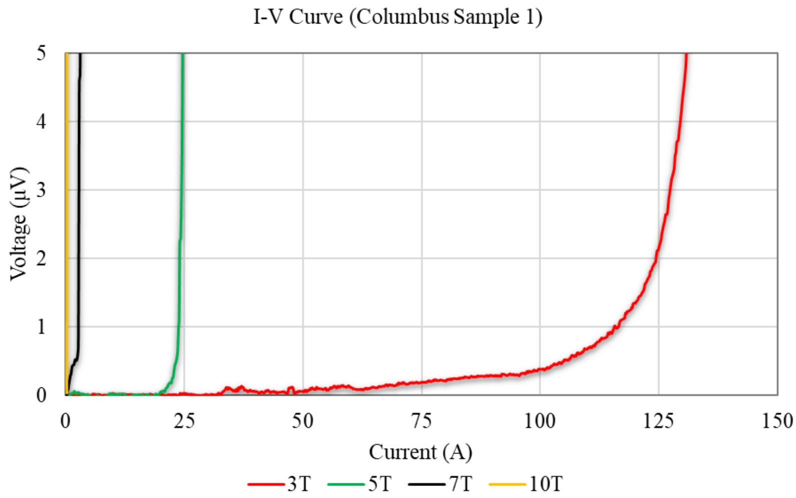


**Figure D.8:** Columbus sample 1 - I-V curve under variable field (3 T - 10 T) under 0 % strain

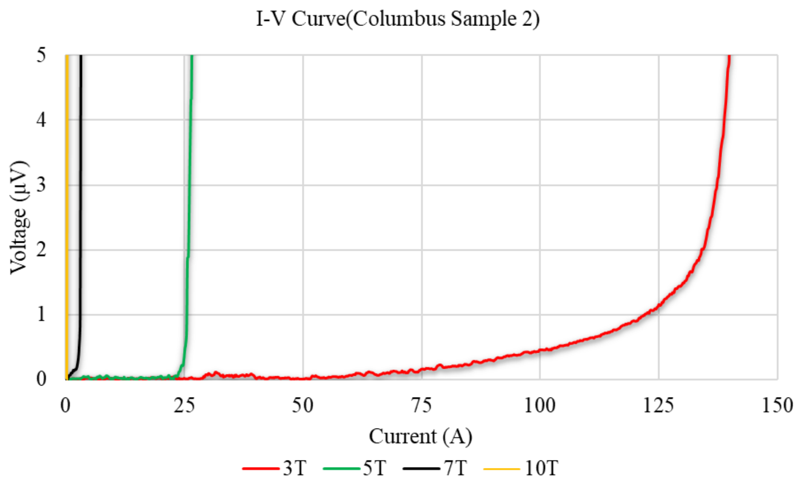


**Figure D.9:** Columbus sample 2 - I-V curve under variable field (3 T - 10 T) under 0 % strain

- I-V curve ; Field=5T; variable strain

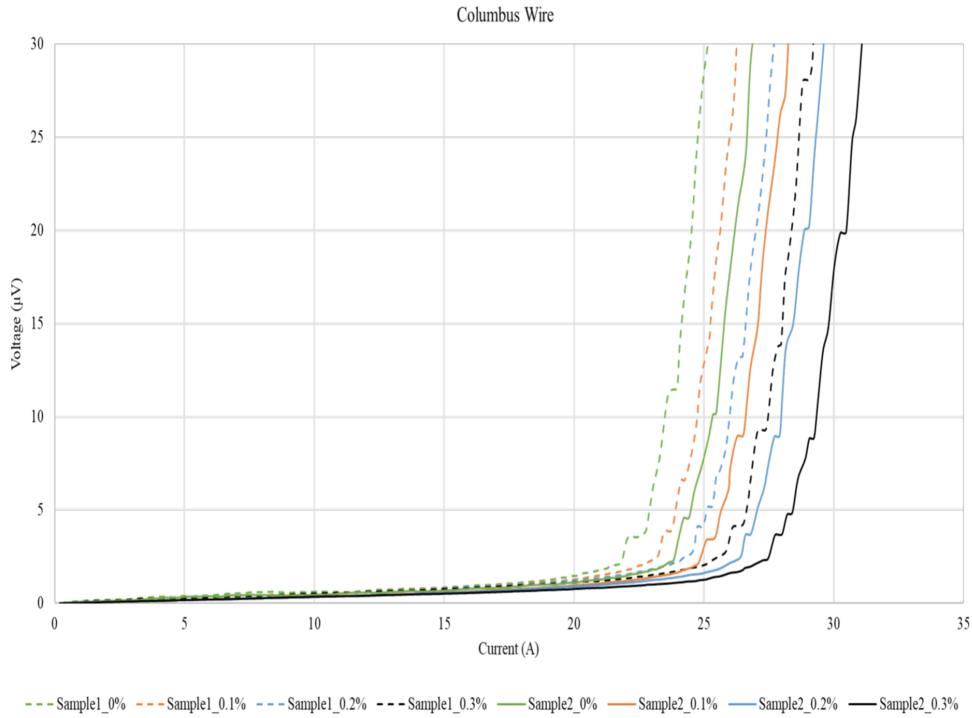


**Figure D.10:** Columbus samples - I-V curve under variable strain and fixed field B= 5 T

D.10 shows the I-V curve of Columbus sample wire under variable strain vary from 0 % to 0.3 % as above 0.3 % we observed a decline in the critical current of the sample wire. Both samples are characterized under external magnetic of 5 T.

- **HyperTech Sample wire**
- $I_c$ dependence due to external field

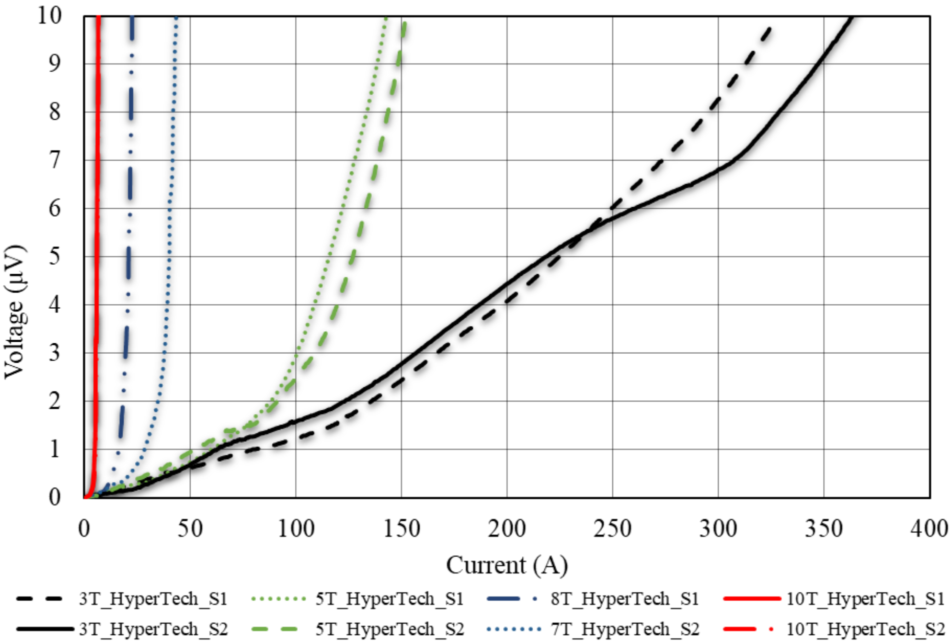


**Figure D.11:** HyperTech samples dependence of external magnetic field on critical current, strain = 0 %

D.11 show a resistive behavior with a linear rise in the voltage one of the reason for such behavior is short test sample of 46 -47 mm with voltage take a distance of around 15mm which does not seems enough for getting the critical current value at criterion of the electric field of 1$\mu$V